High Frequency Ultrasound Measurements of Positions of Optical Fibres for Interstitial Photodynamic Therapy

Master's Thesis
by
Ulrika Malmborg and David Carlström

Lund Reports on Atomic Physics, LRAP 353
Department of Physics, Lund Institute of Technology
Lund, February 2006

February 8, 2006

Abstract

Interstitial photodynamic therapy is a new modality in prostate cancer therapy. Equipment for the therapy is presently being developed by SpectraCure AB and a clinical study is about to begin.

The focus in this thesis was set on positioning optical fibres in tissue from ultrasonic images. The exact positions of the optical fibres is very important to know to be able to do a correct dose plan. Due to the short penetration depth of light, the accuracy of the positioning needs to be on a sub-millimeter level. The goal of this thesis project was set to determine how accurate fibre positioning can be done in ultrasound images.

A fibre positioning algorithm using a fitting of a shape by translational and rotational operations was determined to be the most suitable for the application. Measurements between optical fibres in both a tissue equivalent phantom and in a liver tissue sample yielded a deviation from correct value less than 0,5 mm with a standard deviation of approximately 0,3 mm. Even for a worst case scenario the error will be less than a millimeter.

This thesis project was the first in a new collaboration between the division of Atomic Physics and the department of Electrical Measurements at Lund Institute of Technology and was designed to aid SpectraCure in their development.

Keywords: IPDT, diagnostic ultrasound, prostate cancer

Contents

Chapter 1

Introduction

1.1 Background

At the division of Atomic Physics there is an ongoing project with the aim to treat prostate cancer with light. The procedure is called interstitial photodynamic therapy. The principle is to guide light to the tumor which is medicated in advance with a light sensitive drug, a so called photosensitizer. The light activates the photosensitizer and poisonous reactants are created which kills the tumor cells. The project has generated a spin-off company, SpectraCure AB, which now is in the phase of a clinical study.

The treatment light is guided to the tumor with optical fibres. To reach the prostate the fibres are put in long needles which are inserted in the area between the rectum and the penis. To make sure that the entire tumor is treated a good dose plan is needed. The dose plan will give the amount of light that should be delivered and where to deliver it. It is important to spare healthy tissue as much as possible. The positions of the needles and fibres are monitored with an ultrasound scanner. Light in tissue has a very short range since tissue is highly scattering. This makes it very important to know the positions of the optical fibres exactly, and this has been the focus of this thesis.

Ultrasound is widely used in medicine for diagnostic purposes. Since it does not use ionizing radiation it is regarded as a safe diagnostic tool. The resolution and image quality is high in modern scanners. A great number of transducers are available on the market today. One of them is the transrectal probe commonly used to examine the prostate.

This master's thesis is the first in a new collaboration between the division of Atomic Physics and the department of Electric Measurements at Lund Institute of Technology. The division of Atomic Physics has provided expertise

in the field of photodynamic therapy and how light interacts with matter. The department of Electric Measurements has provided expertise in the field of ultrasound.

1.2 Goal

The goal with this master's thesis is to see how accurately the fibre positions can be determined with the means available during treatment, preferably on a sub-millimeter level. The means at hand are an ultrasound scanner and a computer.

The project is designed to aid SpectraCure AB in their development of an interstitial photodynamic therapy system for prostate cancer treatment.

1.3 Scope of Thesis

The thesis work includes:

- producing tissue equivalent phantoms
- characterizing phantom material both acoustically and optically
- image analysis

The experimental work should be as similar to clinical conditions as possible. In a clinic a transrectal probe is used which has a curvilinear array for looking at cross sections of the prostate. Therefore a curvilinear array is an obvious choice for the experiments.

The thesis work also includes novel experiments where Magnetic Resonance Imaging is used to locate fibres in tissue.

1.4 Outline

The thesis starts with a theory chapter, Ch. 2, where the following aspects are treated: anatomy of the prostate, prostate cancer, tissue optics, photodynamic therapy, basics of ultrasound physics and diagnostic ultrasound. In Ch. 3 the instruments used for the different experiments are listed. Ch. 4 documents the process of choosing a phantom material and the characteristics of the chosen material. The measurements of positions are documented in Ch. 5. The thesis ends with a summary and conclusions, Ch. 6, including a brief discussion on future work.

The measurements of positions produced a large amount of figures, and these can be found in appendix A. In appendix B a list of work responsibilities is shown. During the process of making phantoms a recipe for candle gel phantoms was written. This recipe can be found in appendix C. Appendix D documents novel experiments with the aim to see if optical fibres can be seen in magnetic resonance images. A visit was made to a brachytherapy session which is documented in appendix E. Appendix F, includes MatLab code produced during the project.

Chapter 2

Theory

2.1 The Prostate

The prostate is a glandular organ, approximately the size of a chestnut. It is situated underneath the bladder and surrounds the urethra. The main function of the prostate is to provide a secretion during ejaculation. The posterior surface of the prostate is set close to the rectum. The prostate consists of smooth muscular tissue, elastic connective tissue and is surrounded by a fibrous capsule. The elements of the gland are situated in a way, that they look like clusters of grapes.[1]

The prostate has several lobes:

- The anterior lobe which lies anterior to the urethra.
- The posterior lobe lies posterior to the urethra and inferior to the ejaculatory ducts. When examining the prostate rectally, this is the lobe that is palpated (to palpate means to feel with your hand).
- The two lateral (side) lobes are situated on both sides of the urethra. They constitute the largest part of the prostate.
- The median (middle) lobe is situated between the ejaculatory ducts and the urethra. It is related closely to the bladder.

However, some of these lobes are not well separated antomically.[2;3]

The prostate is relatively small during the childhood, but starts growing during puberty, mainly due to the start of testosterone production. Then, it gets its final size and shape and starts functioning. Around the age of fifty, the testosterone production is generally decreasing, resulting in a degeneration of prostatic tissue. At the same time, the number of gland elements, and thus the size of the prostate tend to increase. This phenomenon is called

benign prostatic hyperplasia or BPH, and the main symptoms are difficulties to urinate and to empty the bladder.

2.2 Prostate Cancer

For men, prostate cancer is by far the most common form of cancer. The incidence is some 7000 cases per year for Sweden. Prostate cancer is, however, strongly dependent on age. Practically no men younger than 40 years of age are diagnosed, and over half of the diagnosed men are over 72. The occurrence of prostate cancer varies between geographical areas and ethnical groups. The incidence for African Americans is considerably higher than for people of Asian descent. The incidence of prostate cancer is the highest in the Western European and North American countries. It can be noted as an example that Japanese people that emigrate to the USA when they are young have a considerably higher risk of developing prostate cancer, than if they would have stayed in their native country. This, along with several other studies, suggest that the Western way of life, with overweight and a high intake of dairy products, is not entirely healthy. As other countries have introduced Western food, for example more animal fat, the incidence of prostate cancer has increased[4;5]. Several studies have also shown that prostate cancer is hereditary. This means that if a man has a brother or a father that developed prostate cancer, the risk of him developing prostate cancer is doubled. If more than one close relative have the disease, the risk increases further. It has also been found that the hereditary form of prostate cancer in general develops about 5 to 10 years before the spontaneous, or sporadic form.[4]

The incidence in the Western world has increased significantly the last couple of decades. This is, in part, due to the fact that the population contains a larger number of elders than before, but also due to the introduction of the prostate specific antigen bloodtest some 15 years ago.

2.2.1 Characterization

Prostate cancer is characterized by the appearance of the tumour tissue on a scale from one to five where one is very much like normal prostate gland tissue, i.e. well differentiated, and five is very different from ordinary prostate gland tissue, i.e. poorly differentiated. This is the so called Gleason Grading scale. The different grades can be seen in figure 2.1. The histopathologist always try to characterize and grade the most common and the second most common growth pattern for the tumour. When combining these patterns in the prostate a Gleason Score is obtained ranging from 2 (either a single or

two well differentiated patterns) to 10 (two poorly differentiated patterns). This score gives a lot of information to the treating physician regarding the prognosis of the patient and also which kind of treatment will work.[6]

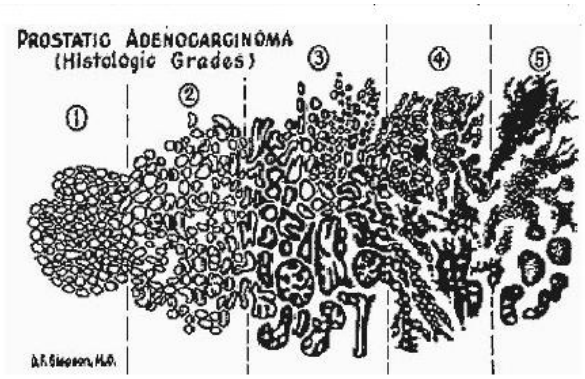

Figure 2.1: Gleason's original drawing of the scale.[7]

Another way of characterizing the tumour is via the TNM-system(*Tumour-Node-Metastasis*)[8]:

T1 : The tumour cannot be felt during a palpation examination and will not show up on an imaging examination.
-T1a: Diagnosis following a TURP (*Transurethral prostatectomy*) with cancer in $<5\%$ of the examined tissue.
-T1b: Diagnosis following a TURP with cancer in $>5\%$ of the examined tissue.
-T1c: Diagnosis from a prostate biopsy.

T2 : Tumour confined to the prostatic gland. Palpable and/or visible in an imaging examination.
-T2a: Tumour confined to 1/2 of a lobe.
-T2b: Tumour confined to 1 lobe.
-T2c: Tumour present in 2 lobes.

T3 : Tumour extending through prostate capsule.
-T3a: Extracapsular growth into connective tissue.
-T3b: Invasion of seminal vesicle(s).

T4 : Tumour either fixed against pelvic wall or directly invading other structures like bladder or sphincter.

Nx : Regional lymph nodes cannot be examined.

N0 : No metastasis found in lymph node.

N1 : Metastasis found in lymph node.

Mx : Spread of cancer cannot be examined.

M0 : No evidence of prostate cancer cells elsewhere in the body found.

M1 : Evidence of prostate cancer cells elsewhere in the body found, usually in the skeleton.

2.2.2 Diagnostic Examination

The examination should always be worked out with respect to the age of the patient and the general condition. Apart from morphological verification of the diagnosis, an adequate characterization with respect to the spread of the tumour should be sought, in order to achieve an optimal treatment plan. The primary diagnostic methods are:

- *Prostate Specific Antigen*, PSA, tests. PSA is a protein that is produced in the epithelials of the prostate. The function of PSA is to transform the semen from a gel state to a liquid state, thus making it easier for the sperm to move about. Some PSA leaks into the blood. In the blood PSA can occur either on its own or in a bond with other proteins. In the event of cancer, the glandular structure is destroyed, and more PSA will be leaked to the blood stream even though the amount produced is less. This means that PSA can be used as a means to diagnose cancer. The problem is, that prostate cancer is not the only reason for more PSA ending up in the blood. When the prostate grows and more glandular cells are produced in the event of benign prostate hyperplasia, more PSA will be produced and the level of PSA in the blood will increase. This is also true for prostatitis. Thus, it is fairly difficult to know what the cause of increased blood PSA level can be, as well as setting a limit with enough specificity concerning the distinction between cancer and other causes. If the limit is set too low, many people that have a latent form of prostate cancer or no cancer whatsoever will be wrongfully diagnosed, meaning that many people will go through further testing as well as be anxious for no reason at all. If, on the other hand, the limit is set too high, the testing will miss several cases of cancer. This is the reason why there is no general PSA-screening procedure in Sweden. A patient with a suspicious PSA level is always examined via a tissue biopsy.[4]

- Palpation, which means that the doctor examines the prostate via the rectal canal. If the prostate feels for example hard or lumpy, a tissue biopsy is taken. Palpation is a somewhat crude method, and it is

difficult to estimate the actual size of the tumour. It is still widely used, in part due to the fact that it is an easily performed examination and also due to the fact that there is not any better method when it comes to actual discovery of a tumour. A PSA test gives a much higher response in terms of patients suspected to have cancer, but those responses are, as stated previously, to a high degree false.[4;5]

- Transrectal Ultrasound guided needle biopsy is used as a follow up test for suspicious cases found with palpation and/or PSA tests. When a curative treatment is considered, a biopsy should always be made. Six biopsies are taken from each patient and histopathologically examined.[4]

2.2.3 Treatment

The expected lifetime of the patient with localized prostate cancer is often crucial when it comes to choosing which treatment that should be used. The patients are often old and have often no symptoms of their disease. A patient with an expected lifetime of no more than ten years have little to gain by receiving curative treatment, and are thus often treated with endocrinological, symptom-guided thearpy. If the patient is about 70 years of age, or less, and otherwise healthy, a curative treatment is often suggested. There are as of now three alternatives of treatment to choose from: prostatectomy, external and internal radiation therapy.

Radical prostatectomy means that the prostate, along with nearby lymph nodes, is surgically removed, thus removing the cancer as well. During this procedure, the patient is under general anesthesia. A catheter is inserted through the penis to the bladder to carry the urine while the area heals. The patient is usually hospitalized for two-three days, has to have the catheter for two-three weeks, and can go back to work after a month or two. The main advantages are that in removing the whole prostate, the risk of residual tumour tissue is considerably reduced. The removed lymph nodes also offer a means to determine how far progressed the cancer is. The main risks are incontinence and impotence. Severe incontinence affect some 10% of the cases. About a third suffer some leakage when for example working out or laughing. A majority of the patients suffer impotence after a prostatectomy. The chance of avoiding impotence is substansially higher if the surgeon can avoid cutting the nerves. The chance of regaining sexual function is also higher if the patient is in his fifties rather than in his seventies.[9]

Radiation therapy means that the prostate is subjected to ionizing radiation. There are two forms: external and internal radiation. External

radiation therapy means treatment with a radiation therapy machine usually for seven weeks, five days a week. For internal radiation therapy, several radioactive seeds are implanted in the prostate. The implant procedure is ultrasound guided as can be seen in figure 2.2. This form of treatment is called brachytherapy and is usually a one-time treatment. The patient comes to the hospital, the implants are placed in the prostate and then the patient can leave. The convalescence time is virtually non-existent for this type of procedure. A description of a brachytherapy procedure is found in appendix E. The side-effects of radiation therapy include urinary and rectal problems. Patients of external radiation therapy sometimes experience tiredness in the end of the treatment. Long-term effects include impotence, which about half the patients suffer, and moderate rectal problems. Incontinence is a rare side effect.

It is diffcult to compare prostatectomy and radiation therapy since no large randomized studies have been made, but results so far indicate that the rate of successful treatments for each kind is about the same. There is, however, a higher degree of uncertainty for radiation therapy since the prostate gland and the lymph nodes are not removed during treatment, meaning that the treating physician can never be sure just how far the disease has spread. This could indicate why the recidivity frequency seems to be a little higher for radiation therapy, but that could also be explained by selection towards more specialized tumours in the patients treated by radiation therapy. Since there is considerable uncertainty concerning whether prostatectomy or radiation therapy is superior and the costs are comparable, the life situation and the desires of the patient has to be taken into consideration when choosing the optimal treatment.[5;9]

Palliative treatment The curative treatment options described above are usually only available if the cancer is localized. If on the other hand the

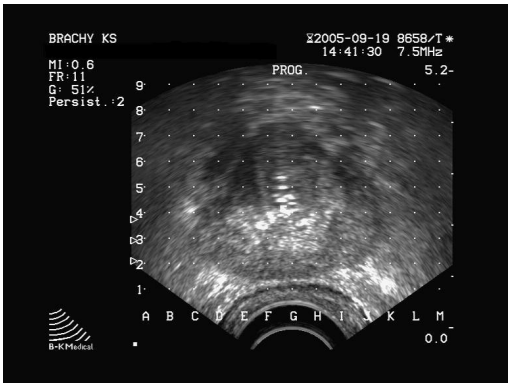

Figure 2.2: Prostate ultrasound during brachytherapy

cancer is spreading outside the prostatic sheath and has metastasized, an endocrinological treatment approach is usually chosen. Endocrinological treatment is not curing, but can give symptomatic and pain relief. This is however strongly connected with the age of the patient and how the patient's general condition is. Sometimes endcrinological therapy is used in combination with radiation therapy. The most important endocrinological treatment options available are bilateral orchiectomy and medical castration. Orchiectomy is surgery where physical castration is achieved. A prostate tumour, at least initially, is dependent on a supply of hormones, which makes orchiectomy often have good effect.

Medical castration on the other hand uses injections of certain hormones, GnRH-analouges, to achieve a similar effect as orchiectomy. The positive side of this approach is that surgery is unnecessary. On the other hand, the injections are very expensive. There are several other hormonal treatments for prostate cancer, all of which suffer from the same disadvantage as GnRH, namely the sheer expensiveness of the drugs and thus the treatment.[4;5]

2.3 Tissue Optics

Light can be described as energy quantas, photons, having both wave and particle properties. For most practical applications the particle approach is sufficient but can not explain phenomena such as diffraction and interference. In general, light will interact with the outermost electrons of the atom or molecule it impinges on. Basically two processes may occur, the photon can be scattered or it can be absorbed. Scattering is quantified with the *scattering coefficient*, μ_s, which is defined as the probability for a photon to be scattered per unit length. Absorption has a corresponding factor, the *absorption coefficient*, μ_a, defined as the probability for a photon to be absorbed per unit length.

Absorption will occur if the impinging photon has an energy corresponding to an enery-gap in the atom or molecule. This results in an excitation of the atom or molecule and from the deexcitation valuable information can be retrieved. The deexitiation can occur through several processes:

Internal conversion where energy is lost through collisions with other atoms or molecules. A non-radiative process.

Fluorescence where a photon with the same or lower energy is emitted depending on if the process is preceded by internal conversion.

Intersystem crossing where a "forbidden" transition between different multiplicity states occur, for example from a singlet state to a triplet state. The process will lead to *metastable*, long-lived ($\mu s - s$), states since

the final relaxation to the singlet ground state is also forbidden. The process has a higher probability in complex molecules.

Phosphorescence where a photon is emitted from a atom/molecule in a metastable state.

Figure 2.3 shows absorption and the different possible deexitation processes in a molecule. Since molecules and atoms have unique energy levels, fluorescence signals will also be unique which can provide valuable information. During the time in the metastable state, there is a high probability for the molecule to collide with other surrounding molecules and atoms and thereby transferring energy to these. This energy transfer is fundamental for photodynamic therapy and also for the action of some laser systems, for example the He-Ne laser.

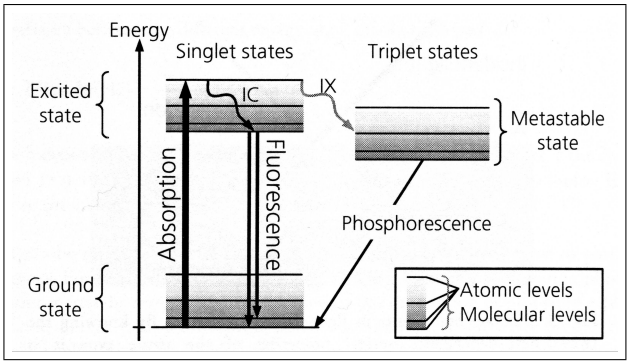

Figure 2.3: Energy level diagram showing absorption and possible energy transfer paths. IC stands for internal conversion and IX for intersystem crossing. Figure taken from Thompson [10].

If the energy of the photon does not match an energy gap, the photon will likely be scattered. Scattering can be *elastic* or *inelastic* depending on if the atom or molecule retains some energy or not. The probability for elastic scattering is much higher than for inelastic. After a scattering event the direction of the photon is likely changed. The directivity can be quantified by the *anisotropy factor*, g.

The following sections will treat how light interacts with turbid media, more specifically, tissue.

2.3.1 Absorption in Tissue

Figure 2.4 shows the absorption coefficient as a function of wavelength for some of the major chromophores in tissue. The gray area between 630 nm and 1300 nm is known as the tissue optical window and indicates where the tissue constituents have their lowest overall absorption. Water is a strong

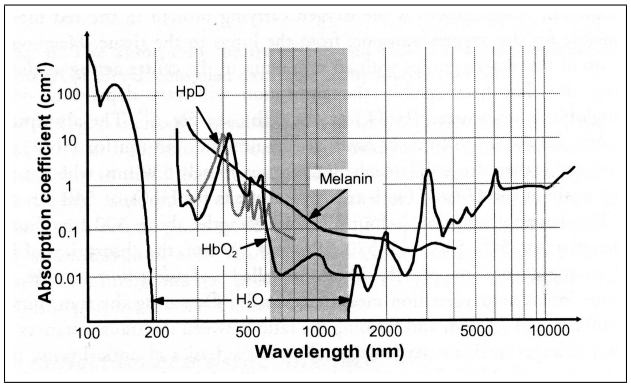

Figure 2.4: Absorption spectra for some of the major chromophores in tissue. Figure adapted from Boulnois[11] and presented in Thompson[10].

absorber in the UV- and IR-regions but does not absorb at all in the visible regime, 400-750 nm. HpD is a denotation for *haematoporphyrin derivative*, a commonly used photosensitizer, which will be further treated in section 2.4.2. Melanin is the chromophore that gives color to the skin, hair and the eye's iris. Due to its high absorption in the tissue optical window, it can cause problems during treatment of superficial skin lesions. The layer containing melanin is often very thin but for some conditions, like malignant melanoma, the layer is very thick making the skin practically impenetrable to light.

The dominating absorber in internal organs is *haemoglobin*, the oxygen carrying protein in the red blood cells. The absorption characteristics of haemoglobin depends on if it is oxygenated or not, where the oxygenated form is denoted HbO_2 and the non-oxygenated form Hb. The difference can be seen in figure 2.5. By measuring transmittance at two wavelengths, one where absorption is equal and one where the absorption differ, and taking the ratio between them, information of tissue oxygenation can be retrieved. This method is used in for example optical pulse oximetry.

2.3.2 Scattering in Tissue

In tissue, scattering occurs by multiple reflections between and within cells and organelles. Major scatterers are cell membranes[13], cell nuclei and mitochondrias[14], the cell's energy producer. Within the optical window, scattering is much higher than absorption, see figure 2.6.

There are mainly two theoretical models on scattering, Mie and Rayleigh. The latter can be applied for scattering against small particles, much smaller than the wavelength of the light. The intensity of the scattered light has a

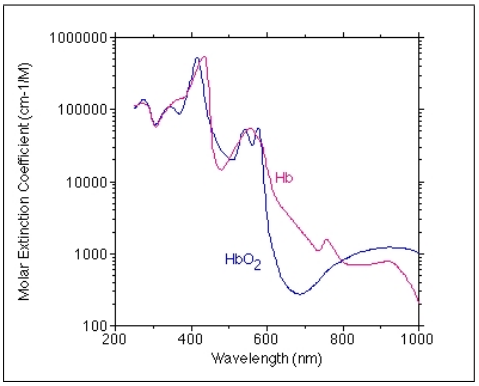

Figure 2.5: Absorption spectra of HbO_2 and Hb. Compiled from a variety of sources by Prahl[12].

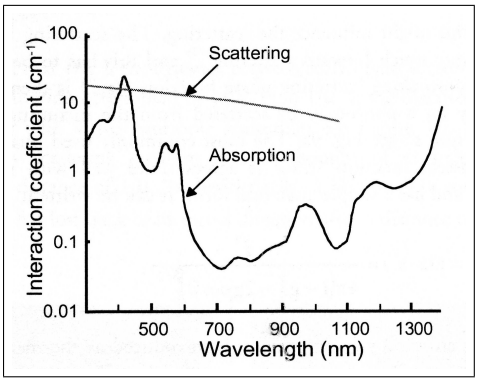

Figure 2.6: Scattering and absorption factors within the tissue optical window. Modified from af Klinteberg[15] and presented in Thompson[10].

$1/\lambda^4$ dependence and is isotropically distributed. Mie scattering is derived from Maxwell's equations and is applied for spherical objects with a size comparable to the wavelength. The intensity is approximately proportional to $1/\lambda^2$ and has a forward directed distribution. The different wavelength dependencies of Mie and Rayleigh scattering can be seen in figure 2.6, where the flatter curve at shorter wavelengths indicates Mie scattering and the steeper slope at longer wavelengths indicates Rayleigh scattering.

Scattering in tissue has been shown to have a forward directed distribution which has to be considered when modeling light transport[16]. The scattering anisotropy factor, g, is defined as the mean value of cos θ, $g = \langle \cos\theta \rangle$, where θ is the angle between the incoming light and the scattered light. The g-factor ranges between -1 to 1, where -1 is total back scattering, 0 is isotropic scattering and 1 is total forward scattering. In tissue the g-factor is found to be in the range between 0,8-0,95[17].

The absorption and scattering coefficients will determine the penetration depth of light in tissue. For shorter wavelengths the scattering is very high and the penetration depth will be short. For longer wavelengths the scattering coefficient decreases and the penetration depth increases. The deepest penetration is found in the near infrared region before water starts to absorb heavily.

2.3.3 Modeling of Light Transport in Tissue

As stated before, light can be seen both as electromagnetic waves and as particles. Light transport with the wave approach can be modeled with Maxwell's equations and is the most fundamental way to describe light transport. The equation is complicated and only a few analytical solutions exist, thereby making simplifications and approximations necessary for most practical applications. Light transportation with the particle approach can be modeled with energy conservation, for example using the transport equation. The latter approach of light is the most used in tissue optics. The transport equation is the basis of several models and is briefly outlined below.

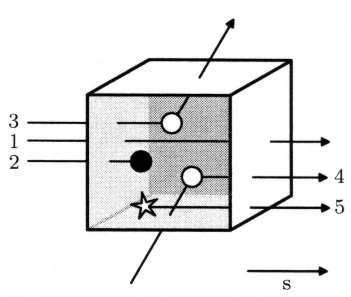

Figure 2.7: Schematic description of the different contributions to the transport equation. Taken from Abrahamsson[18].

In light flow applications the equation is usually expressed as a continuity function of the radiance, $L(\mathbf{r}, \mathbf{s}, t)[W/m^2 \cdot sr]$, the light intensity per unit area and solid angle. The different contributions to the transport equation can schematically be described by looking at a small volume element as in figure 2.7. The contributions are:

1. Light transmitted in the s direction.
2. Light absorbed.
3. Light scattered away from the direction s.
4. Light scattered into the direction s.
5. Light sources within the element.

These five parts leads to the following equation, the transport equation.

$$\frac{1}{v}\frac{\partial L(\mathbf{r},\mathbf{s},t)}{\partial t} = \underbrace{-\mathbf{s}\cdot\nabla L(\mathbf{r},\mathbf{s},t)}_{1} - \underbrace{(\mu_a+\mu_s)\cdot L(\mathbf{r},\mathbf{s},t)}_{2,3} + \\ + \underbrace{\mu_s\int_{4\pi} L(\mathbf{r},\mathbf{s}',t)p(\mathbf{s},\mathbf{s}')d\omega'}_{4} + \underbrace{Q(\mathbf{r},\mathbf{s},t)}_{5} \tag{2.1}$$

The transport equation can be solved both analytically and numerically after some simplifications, and can be used to simulate the light transport using for example Monte Carlo simulations.

2.4 Photodynamic Therapy

Photodynamic Therapy, PDT, is a treatment used for various localized lesions. It requires three components: *therapeutic light*, a *photosensitizer* and *tissue oxygen*. The wavelength of the therapeutic light is matched to an absorption peak in the sensitizer which is designed to accumulate to a higher degree in diseased than in healthy tissue. The light will activate the sensitizer and one of the following two reactions may occur.[10]

Type I reaction where energy from the photosensitizer transfers directly to atoms or molecules in the surrounding forming free radicals.[10]

Type II reaction where the sensitizer reacts with naturally existing triplet oxygen ($O_2(^3\Sigma_g)$) in the tissue and forms highly oxidative singlet oxygen ($O_2(^1\Delta_g)$).[10]

The type II reaction is much more efficient since protective mechanisms in the cell often can handle free radical formations, but not singlet oxygen[19]. For an effective treatment the supply of oxygen is therefore essential.

The reactions will induce *necrosis* and/or *apoptosis* depending on the subcellular location of the sensitizer[10]. Necrosis is cell death caused by progressive degradative action of enzymes while apoptosis is programmed cell death signaled from the nuclei. Apoptosis is in normal cells dictated by the age and state of health of the cell but is in cancer cells put out of action. Cancer cells can also be killed by targeting the often extensive vasculatory system that supplies the tumor with blood and other nutrients. It is found that damage to circulation is particularly lethal to rapidly growing cells, such as cancer cells. The vasculature can be targeted by putting high levels of sensitizer in the blood plasma, for example with an intravenous injection, which will

effect the membranes of the *endothelial cells* that covers the inside of blood vessels. As a second effect, membrane damage will release inflammatory and immunostimulating mediators which starts series of events that further induces cell death.[20]

After transferring its energy to the surrounding the photosensitizer returns to the ground state and can be activated again. This process is however not endless, due to that the generated singlet oxygen also can oxidize the photosensitizer. This process is called *photobleaching* and reduces the risk of over-treating a lesion.[10]

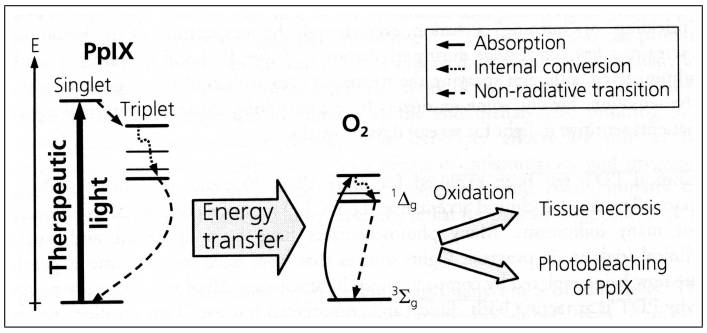

Figure 2.8: A schematic view of the physical mechanism of PDT using protoporphyrin IX, a commonly used photosensitizer. Taken from Thompson[10]

In figure 2.8 a schematic view of PDT using *Protoporphyrin*, PpIX, as a photosensitizer is shown. The therapeutic light will excite the sensitizer and by intersystem crossing it can be transferred to a metastable state. From this state it might deexcite by transferring its excess energy to an oxygen molecule in the surrounding. The oxygen molecule will then form the highly oxidative singlet oxygen and induce either tissue necrosis or photobleaching.[10]

The tumor is rapidly destroyed and damage to surrounding healthy tissue is healed within 6-8 weeks with usually good cosmetic result. The selectivity of the treatment is optimized through several factors.[21]

- Focused light delivery to treatment area minimizes irradiation to surrounding healthy tissue. Often different fiber-optical setups are used. The high scattering factor of tissue gives a very short penetration depth that further increases the selectivity.[21]
- Selectivity of photosensitizer to diseased tissue. The exact mechanisms behind this are not fully understood but contributing factors could be poor lymphatic drainage, leaky vasculature, decreased pH and/or other physiological abnormalities in tumors.[21]
- Short life time of the singlet oxygen prevents the toxic oxygen to wander into surrounding healthy tissue.[21]

The use of light, most often in the visible region, has its advantages and disadvantages. The major advantage is that it is non-ionizing and therefore has no dose limitation, that is, the procedure can be repeated until a satisfactory result is reached. It does not influence the collagen structure in the tissue as ionizing radiation and the risk of inducing new tumors is minimal. The disadvantage lies in the limited penetration depth of light. The penetration depth increases with wavelength but will still only be a few millimeters. The wavelength must also be chosen so that the major absorption will occur in the photosensitizer and not in other molecules, like hemoglobin.

2.4.1 Interstitial Photodynamic Therapy

Interstitial photodynamic therapy, IPDT, is a development of the original PDT treatment, which makes a greater number of lesions with varying sizes and locations possible to treat. The original treatment is confined to superficial, thin lesions due to the short penetration depth of light. It is used mostly to treat different kinds of skin lesions, such as basal cell carcinoma and actinic keratosis. In IPDT multiple optical fibers are inserted into the lesion, making it possible to get light into larger and/or deeper lying lesions.

The prostate is seen as a good candidate for IPDT. The organ is small, making it possible to treat the whole lesion. Placement techniques for positioning fibers can be adopted from brachytherapy, a well established treatment method. There is a large group of patients suitable for the treatment and the structure of the gland is not totally destroyed.[22]

One of the major problems that needs to be solved is dosimetry, the amount of light and sensitizer that should be administered, and the positioning of the fibres. The dosimetry is very dependent on the optical parameters of the tissue, since they determine the propagation of the light. Unfortunately the parameters tend to change during the course of treatment, and between patients[10]. Often the changes causes a decrease in penetration depth and to make sure that the whole volume gets treated, a correction of the treatment time is needed[10]. Why the parameters change is not fully understood, but a possible explanation could be that the consumption of oxygen during treatment decreases the level of HbO in favor for the more absorbing Hb[23]. Another explanation could be that the circulation in small vessels in the tissue gets damaged during treatment[10]. It is also important to monitor the oxygen concentration to make sure that enough oxygen is present for the treatment to work. These factors imply that measurements during treatment is needed. One method used is to pause the treatment and make measurements, for example, every minute. After each measurement the dosimetry is recalculated using the new parameters. This procedure has another advantage, by pausing the treatment new oxygen can enter the tissue and the

efficiency of the treatment can be raised.

SpectraCure has implemented the treatment in the following way:

1. The geometry of the prostate is estimated using different imaging techniques, such as ultrasound and CT.
2. The positions where the optical fibres should be inserted for optimal treatment is calculated.
3. The fibres are calibrated and inserted through brachytherapy needles. They are monitored with ultrasound.
4. The actual positions of the fibres are determined.
5. Optical parameters, drug concentration and oxygen levels are measured.
6. An optimal dosimetry is calculated.
7. The treatment is initiated.
8. After a few minutes the treatment pauses and new measurements are made. The dosimetry is recalculated with the new parameters.
9. The treatment continues.
10. After an additional few minutes the treatment pauses again, new measurements are made and dosimetry is recalculated.
11. The treatment continues and the procedure repeats itself until full treatment time is reached.

2.4.2 Photosensitizers

A good photosensitizer should have the following characteristics:

- High absorbance in the far red region allowing treatment in thicker lesions.
- High selectivity between healthy and diseased tissue.
- Short build-up time in the tissue.
- High clearance rate.
- Low toxicity.

The first photosensitizer used in PDT was *haematoporphyrin derivative*, HpD. It has strong absorption in the red at 630 nm which is used for activation, but has several disadvantages. The selectivity is low, approximately 2 - 3 : 1 (diseased to healthy tissue), it has a long build-up time, 48-72 hours,

and has a long clearance time, 4-6 weeks[10]. *Porfimer sodium* is based on HpD, with some of its non-active components removed, and was the first drug which received approval for use in PDT. Its commercial name is Photofrin®, and is still used (as of august 2004) especially for non-dermatological tumors such as: advanced and early-stage lung cancers, superficial gastric cancer, cervical cancer, esophageal adenocarcinoma and bladder cancer. However, PDT is not a widely used treatment modality for these lesions.[21]

Aminolaevulinic acid, in short ALA, is a pre-cursor to another porphyrin photosensitizer, *protoporphyrin IX*, PpIX. ALA itself is not photosensitive at all, but takes part in the *haem cycle*, a biochemical process occuring in all living cells that produces haem. Haem is found in most oxygen carrier proteins. ALA can also be used as a fluorescence marker, fluorescing at 635 nm and 705 nm when excited with 405 nm light. The wavelength of light used for ALA-PDT is 635 nm. The fluorescing characteristics makes it possible to monitor the build-up of the sensitizer before the treatment is initialized. For topical administration maximum build-up is reached 4-6 h after application and is fully cleared within 48 h. During irradiation the PpIX will be consumed and produce photo products that fluoresce broadly at 670 nm. This feature can be used to measure the photobleacing.[10] ALA is approved (as of 2001) to be used in treatments of actinic keratosis, superficial basal-cell carcinoma and basal-cell carcinoma[21].

Chlorins is another group of photosensitizers that are chemically similar to porphyrins. Its absorption spectra is shifted towards longer wavelengths. A clinically used chlorin is *meta-tetrahydroxyphenylchlorin*, mTHPC, also knowned as Temoporfin or Foscan®. It is activated at 652 nm and has shown to be effective already at low doses, but has a low selectivity, slow build-up time, about 96 h, and a long clearance time, 3-6 weeks.[10]

HpD, porfimer sodium, ALA and mTHPC have all been used in clinical studies of PDT for prostate cancer. WST09 (TOOKAD) and motexafin lutetium are two other sensitizers also tried in clinical studies. WST09 is activated with 763 nm and motexafin lutetium with 732 nm.[22].

TOOKAD is interesting in the way that it has a very high production of singlet oxygen and is cleared from the blood stream after only a few hours. This sensitizer is not water soluble and a vehicle, a sort of capsule that encapsulates the drug until it reaches its intended destination, must be used for administration. TOOKAD does not penetrate the cancer cells and the treatment is therefore targeted at the prostate vasculature. Irradiation occurs when maximum concentration in the vasculature is reached which is within a few minutes after administration. The drug levels are hard to monitor since TOOKAD has negible fluorescense but due to the rapid clearance, drug and light delivery occurs practically simultaneously, and makes adjusting drug concentration during treatment possible.[24]

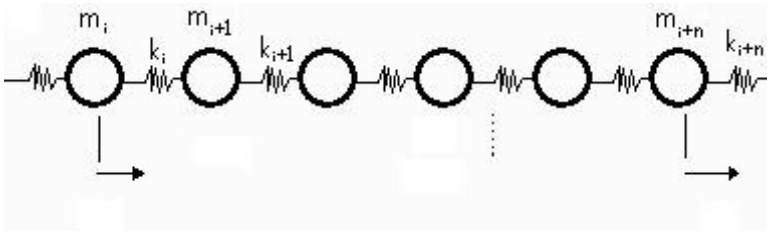

Figure 2.9: Linear lattice

2.5 Ultrasound Physics

A sound wave can generally be described as a propagation of a mechanical disturbance through a medium. The wave is longitudinal, meaning that the disturbance is in the same direction as the propagation. Consider a linear lattice, as shown in figure 2.5, of equal masses, m, coupled with springs of equal constants, k. When one of the masses, m_i is subjected to a force in the direction of the array, it will be displaced and its spring, k_i, compressed. The spring k_i will then subject the mass m_{i+1} to a force, which in turn displaces m_{i+1}, compresses k_{i+1} and so on. The result will be a wave propagating through the mass-spring array with a speed c dependent on the mass m and the spring constant k. The speed c is proportional to k and inversely proportional m. Formulating this in more general terms gives that the speed of sound in a medium is dependent on the density ρ and the compressibility κ of the medium according to

$$c = \sqrt{\frac{1}{\rho\kappa}} \tag{2.2}$$

The acoustic impedance, Z, is defined as the fraction of the driving force, i.e. the acoustic pressure, p, and the velocity response, i.e. the particle velocity, $\dot{s}$ as

$$Z = \frac{p}{\dot{s}} \tag{2.3}$$

which can be written as

$$Z = \rho c = \sqrt{\frac{\rho}{\kappa}} \tag{2.4}$$

The acoustic impedance for a medium can be interpreted as how easy it is for particles in the medium to start oscillating when subjected to a force.[25]

2.6 Diagnostic Ultrasound

When a sound wave is incident on a boundary between two media with different acoustic impedance, a fraction of the wave will be reflected and the

rest transmitted. The amount that will be reflected/transmitted is dependent on the difference in acoustic impedance between the two media. If the difference is small, most of the wave will be transmitted and vice versa. This property is the basis of diagnostic medical ultrasound. Most human tissue, except bone, has similar density and speed of sound. There are however small differences in Z between different tissue types. This means that it is possible to send an ultrasound pulse in to the body, echoing each time it passes a tissue boundary, as can be seen in figure 2.10. Detecting the echoes and knowing the approximate speed of sound in the tissue makes it possible to make an image of the scanned tissue. This is a fast and fairly inexpensive imaging technique. It, however, suffers from several degrading and limiting factors that effect the image quality.

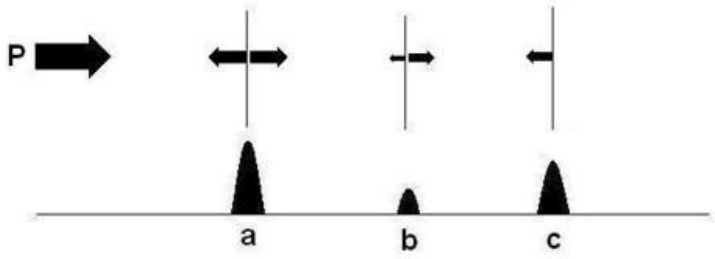

Figure 2.10: An ultrasound wave propagating through tissue. A large echo amplitude indicates a large difference in acoustic impedance between materials and vice versa.

2.6.1 Limiting Factors

The limit of the lateral resolution is the beam width, as shown in figure 2.11. Two objects appearing in the beam at the same time can not be resolved. The beam itself is the narrowest in the focus point and the largest close to and far away from the transducer, making the lateral resolution better in the focus and widening objects far from the focal point.[26]

The axial resolution on the other hand depend strongly on the pulse duration. Pulses with long durations will interfere when reflected from objects closely spaced axially, as shown in figure 2.12. There are two ways to improve axial resolution, either by shortening the pulse duration or by increasing the sound frequency. Both methods yield a shorter pulse. Short pulses can resolve objects closer together, meaning an increased resolution.[26]

Commercially available ultrasound scanners assume the general speed of sound in tissue to be 1540 m/s. This is an approximation since different

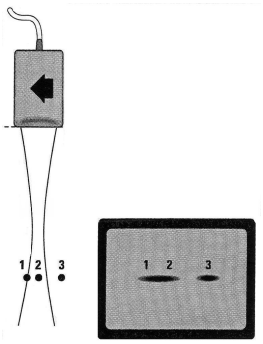

Figure 2.11: Limits of the lateral resolution. Taken from Zagzebski[26].

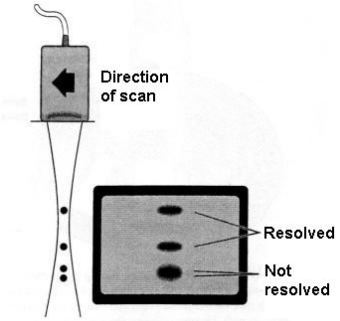

Figure 2.12: Limits of the axial resolution. Taken from Zagzebski[26].

tissues often have different speeds of sound. Human low-fat liver for example has a speed of sound of 1608 m/s[27] at 37°C and fat 1450 m/s. Tissue that has a speed of sound which differ significantly from 1540 m/s will give errors in the ultrasound image, due to the difference in speed of sound as well as refraction. Structures in tissue with lower speed of sound will appear in the image as deeper in the tissue and vice versa. Other degrading factors include multiple reflections.[25;26]

2.6.2 Speckle

The grainy structure apparent in figure 2.13 is a typical feature of an ultrasound image. It is the same phenomenon that makes a laser spot on a wall appear grainy, and is referred to as speckle. Speckle is often treated as a kind of noise, but it is in fact not random. Two ultrasound images taken under exactly the same conditions will yield the same speckle pattern. If the pattern is studied closely, it can be seen that the average grain size is of the same order as the resolution axially and laterally. Scatterers present in the tissue/material studied that are smaller and/or situated closer than

one pulselength (the resolution) will not be possible to resolve. Echoes from these structures will instead interfere, making the final echo response complicated and containing information which does not accurately describe the tissue at that scale, i.e. the echoes does not accurately represent placement of structures. This interference gives rise to the grainy structure. Speckle is therefore an interference phenomenon and not noise. Speckle is frequency-dependent, which means that the appearance and brightness of the grains will change with frequency.[25]

Figure 2.13: Speckle pattern in a tissue phantom

Speckle is thus an unavoidable feature of ultrasound imaging. It is often desirable to reduce speckle and enhance the true features of the image. Since speckle is frequency-dependent, one way to do so is to add images taken with different frequencies, averaging the interference pattern and thereby reducing the influence of speckle. Another way of reducing the speckle pattern is to get a series of images, where the transducer has been moved a certain distance between each image and average. Both of these approaches rely on adding uncorrelated images for reduction of speckle.

Chapter 3

Instrumentation

The chapters involving experiments are chapter 4, The Phantom, and chapter 5, Measurements of postions. Instruments used in these experiments are listed below.

3.1 The Phantom

Choice of material

- Ultrasound scanner Philips HDI 5000
- Philips L12-5 MHz 38 mm linear array transducer

Acoustic characteristics of candle gel

- Two 5 MHz transducers, diameter 6,35 mm, produced at the department of Electrical Measurements
- A 2 MHz transducer, diameter 12 mm, produced at the department of Electrical Measurements
- Pulse reciver, Panametrix TDS 5052PR
- Oscilloscope, Tektronix TDS 1002

Optical characteristics of candle gel

- He-Ne laser, Laxtronic model: CI-220-POL
- CCD-camera, Hamamatsu model: ORCA-ER
- Timeresolved spectroscopy system

3.2 Measurements

- Ultrasound scanner Philips HDI 5000
- Philips C5-2 MHz curved array transducer

Chapter 4

The Phantom

A part of the project was to find a suitable phantom material. The perfect material should have the following characteristics:

- Acoustic properties comparable to prostate tissue
- Highly light scattering comparable to tissue making optical experiments possible
- Easy to handle
- Reusable

On the Ultrasonics Symposium 1993, Parker et.al.[28] presented a study of ultrasonic properties in human and canine prostate. In this study the speed of sound in human prostate tissue was estimated to 1561 ± 22 m/s and the attenuation to $0,78 \pm 0,24\ dB/MHz \cdot cm$.

4.1 Methods

The experiments were divided into three parts. The first part was aimed at finding a suitable phantom material. Two different base materials were invesigated, Agar and candle gel.

Agar is a well known material and is commonly used for ultrasound phantoms. Candle gel is not used as much for phantoms and its characteristics were therefore further analyzed.

The second part analyzed the acoustic characteristics of candle gel. Attenuation and speed of sound were measured.

The third part analyzed the optical characteristics of candle gel. The aim was to see if candle gel could be a candidate for phantoms for optical exper-

iments. The optical properties were measured with two different methods, one spatially and one time-resolved method.

4.1.1 Choosing a Material

Available base materials were Agar and candle gel. Agar is a galactose polymer, a hydrocarbon, obtained from the cell walls of a red algae. Agar is most frequently used as a culture medium in microbiological applications, but is also found in food, for example in ice cream and as a vegetarian gelatin substitute. Candle gel consists of paraffin oil and softening chemicals. The gel was bought from Joel Svenssons Vaxfabrik [1].

The test phantoms were evaluated by comparing ultrasound images with an image recorded of tissue, in this case a piece of pork cutlet. For some of the phantoms an estimation of the speed of sound was made.

Scatterers and absorbers were added to the base material. The mixtures were then cast in a box with three compartments, each $3 \times 3 \times 6$ cm.

12 g of Agar, in powder form, was dissolved in 0,3 l unionized water. For conservation purposes a teaspoon of sodiumbenzoate was added. The mixture was put on a hot plate with a magnetic stirrer at low speed and covered with aluminium foil. The mixture was heated to 85°C, where Agar has a hysteresis point. Graphite was then added with the intention to produce three test phantoms with concentrations 40, 80 and 120 g graphite per liter. The three compartments were estimated to hold 0,05 l each. To obtain a concentration of 40 g/l, $40 \cdot 0,3 = 12$ g graphite was added to the mixture. After careful stirring, trying not to create any air bubbles, the mixture was gently poured into the first compartment until it was filled. To raise the concentration in the mixture to 80 g/l another $40 \cdot 0,25 = 10$ g of graphite was added and the second compartment was filled. Before filling the last compartment, the concentration in the mixture was raised to 120 g/l by adding another $40 \cdot 0,20 = 8$ g of graphite to the mixture. The phantoms were left over night to harden.

The candle gel was delivered in a gelantineous form. An appropriate amount for the three compartments was put in a glass jar and melted in a water bath. Approximately 1 ml of glass beads was added when the gel had melted. The glass beads had a diameter of 70-90 μm. The mixture was then carefully poured into the first compartment.

For the remaining compartments graphite, appoximately 4 g, was added to the mixture. The compartments were then filled. This was done to see how

[1] www.joelvax.se

much a small amount of absorber affects the outcome. The phantoms were left over night, and the material resumed its gelantineous state.

In a second experiment with candle gel, three different materials were added. The added substances all had high optical scattering coefficients. The goal with this experiment was to produce test phantoms with optical properties similar to tissue. Candle gel with glass beads is too transparent and candle gel with graphite is too absorbent. The chosen materials were: TiO_2, milk and polystyrene micro particles. The polystyrene micro particles had the size 1 μm, were white and were dissolved in an unknown solution. The concentration was 25 mg/ml.

For the Agar + graphite, candle gel + glass beads and candle gel + TiO_2 phantoms, the speed of sound was estimated with a simple experiment. An ultrasound transducer was held in a fixed position by a rack. The phantoms were placed in a glass bowl on a small table with adjustable height. According to the manual the ultrasound scanner assumes 1540 m/s as the speed of sound. With the distance measurement feature on the scanner, the distance between the front and the back of the test phantoms were measured. This distance was then compared to a measurement with a slide caliper. The speed of sound was estimated using:

$$v = assumed\ speed\ of\ sound \cdot \frac{real\ distance}{distance\ shown\ on\ scanner} \tag{4.1}$$

4.1.2 Acoustic Characteristics of Candle Gel

The attenuation was determined for pure candle gel without any added scattering or absorbing material and for candle gel with various concentrations of glass beads. The test phantoms were cast in a box with three compartments each with the size $3 \times 3 \times 6$ cm. In total six test phantoms were manufactured. Three with candle gel + glass beads and three with pure candle gel. In the production of the candle gel + glass beads phantoms, a lid was put on the box and the box was mounted on a small motor which made the box rotate. The rotation speed was approximately 2 rpm and the intention was to prevent the glass beads from sinking.

The measurement setup consisted of a water tank, two 5 MHz transducers and a holding device for the phantoms. One of the transducers was connected to a function generator emitting a short sine wave burst at 5 MHz, and the other was connected to an oscilloscope. The holding device was needed to keep the phantom in place since they float in water. The water in the tank was used as contact medium between the phantom and the transducers.

The transducers were aligned in the water tank and the phantom was placed in between. The phantom was placed so that the signal path length through

the phantom was 3 cm and the transmitted signal, displayed on the oscilloscope, was stored. The phantom was then turned so that the signal path length through the phantom was 6 cm and the transmitted signal was stored.

The two signals were Fourier transformed separately and the difference between them was logarithmized to obtain a dB-scale. These calculations provided a plot on the amplitude, in dB, as a function of frequency.

$$amplitude\ (dB) = 20 \cdot \log_{10}\left(\frac{fft(signal\ 3\ cm)}{fft(signal\ 6\ cm)}\right) \tag{4.2}$$

The attenuation can then be obtained from the slope of the amplitude curve at the frequency of the emitted signal. This was done by fitting a first degree polynomial to a small area around 5 MHz, and from this extracting the slope. This value was then divided by the difference in signal path length in the phantom, in this case 3 cm.

The speed of sound was measured with pulse echo technique. A plexiglass box with inner dimensions $10 \times 10 \times 10$ cm was filled with candle gel + glass beads. A 2 MHz transducer connected to a transceiver and an oscilloscope was put against one of the walls of the box, and the echoes returning to the transducer were studied. The time between the echoes from the inner walls was measured. This corresponds to the time it takes for the sound to travel back and forth in the material. The echo reference points were the second zero crossings of the pulses. With the distance known, the speed could easily be calculated.

4.1.3 Optical Characteristics of Candle Gel

For the experiments a phantom with candle gel and TiO_2 was produced. TiO_2 was used as scatterer for light. It is the substance that makes white paint white and is a often used scatterer in phantoms for optical measurements. Glass beads could not be used since they do not give the diffuse light that characterize tissue. The phantom was milky white, although the concentration of TiO_2 was unknown.

The intensity of light in turbid media is dependent on the distance from the light source, r, and the optical characteristics of the material. Taking a picture with a CCD camera of the phantom with a light source inserted, and analyzing how the intensity diminishes with distance, should therefore give an estimation of the optical characteristics for the material. This spatially resolved technique was the first method used.

The relation between intensity and distance from light source can be ex-

pressed as:

$$I \sim \frac{e^{-\mu_{eff}\cdot|\mathbf{r}|}}{|\mathbf{r}|} \tag{4.3}$$

where

$$\mu_{eff} = \sqrt{3\mu_a(\mu_a + (1-g)\mu_s)} = \sqrt{3\mu_a(\mu_a + \mu_s')} \tag{4.4}$$

A sketch of the setup is seen in figure 4.1. The He-Ne laser operated at 632 nm. The light was coupled into an optical fiber which was guided into the phantom through a brachy needle. Images of the lit-up phantom were taken with the CCD-camera with ambient light sources turned off. Three images were stored, one live-image, one averaged over ten images and one averaged over 20 images. An image of a ruler was also taken. The images were transferred to MatLab for analysis.

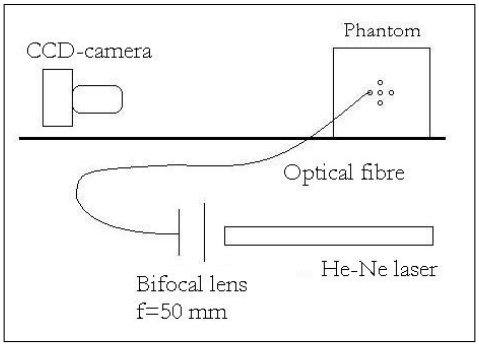

Figure 4.1: Setup for measurement of optical properties with the spatially resolved method.

The point of maximum intensity in the image was located and this point was set to be the point directly above the light source. A cross section, with this point in the middle, was generated and a plot of the intensity as a function of the pixels could be drawn. With the image of the ruler the size of a pixel was determined and the pixel numbers was transformed to a distance from the source, see figure 4.2. The logarithm of the intensity was then plotted against the distance from the source. By taking the logarithm of the intensity, equation 4.4 will transform to:

$$\ln I \sim -|\mathbf{r}| \cdot \mu_{eff} - \ln|\mathbf{r}| \tag{4.5}$$

This is a straight line, and therefore a first degree polynomial was fitted to the curve. From the slope of the fitted curve μ_{eff} could be extracted.

The second method to measure the optical characteristics was time-resolved spectroscopy. The basic principle is to emit a very short laser pulse and then measure the time until a photon reaches a detector. This is done for many

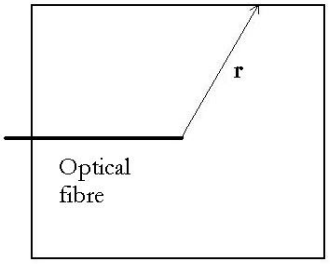

Figure 4.2: The geometry seen from above, where **r** is the distance from the light source to the surface. The light source is in this case the tip of the inserted optical fibre.

pulses and a distribution of arrival times is eventually recorded. The shape of this distribution is dependent on the optical properties.

The measurements were done with a system that has been constructed at the division of Atomic Physics for measurements of optical properties in human tissue. This system measures at four different wavelengths: 660 nm, 785 nm, 910 nm and 974 nm. The optical properties are extracted from the distribution curve by iteratively changing the absorption and scattering coefficients of a theoretical curve until it coincides with the measurement data.

Measurements were made with light source and detector 10, 15, 18 and 20 mm apart. Refractive index for paraffin oil is 1,48[2].

Both methods uses the diffusion equation to extract optical properties from measured data. The diffusion equation is a simplification of the transport equation, see equation 2.1, valid for diffuse light. For diffuse light $\mu_a << \mu_s$, which is the case for most turbid media.

4.2 Results and Discussion

4.2.1 Choosing a Material

The following test phantoms were produced:

1. Agar + graphite, 40g/l
2. Agar + graphite, 80g/l
3. Agar + graphite, 120g/l
4. Candle gel + glass beads

[2]http://www.photometer.com/en/abc/abc_015.htm 20051212

5. Candle gel + glass beads + graphite
6. Candle gel + TiO_2
7. Candle gel + milk
8. Candle gel + micro particles

The ultrasound images recorded on the Agar + graphite phantoms showed a homogeneously distributed speckle pattern with the same size as in the images of the pork cutlet. The attenuation was comparable to the cutlet and no visible air bubbles could be seen in the phantom. There was less mixture left than anticipated in the mixing jar, indicating that the concentrations were probably higher than intended. This can be due to evaporisation during heating.

The candle gel + glass beads phantom also had a speckle pattern similar to tissue. The glass beads were not homogeneously distributed, since they tended to sink during the hardening process.

The candle gel + glass beads + graphite phantoms had a lot of bubbles and a somewhat larger speckle pattern. Line patterns were seen on the phantom, indicating that the graphite did not distribute homogeneously.

The candle gel + TiO_2 phantom had lots of bubbles probably due to a faulty manufacturing process, or that some reaction occured between the TiO_2 and the paraffin oil. The TiO_2 was not homogeneously distributed in the gel.

The candle gel + milk phantom was dismissed at an early stage since the milk and gel did not mix. The most probable explanation is that milk contains water which does not mix with oil.

The candle gel + micro particles were also dismissed since they did not mix. The solution the particles were dissolved in probably contained water.

The experiments showed that Agar + graphite and candle gel + glass beads were the most suitable materials. They did, however, not have the wanted optical properties. A second attempt was made to make a better candle gel + TiO_2 phantom, using a different approach in the production process. This time the TiO_2 was mixed in a small amount of gel before adding more gel to fill up the compartment. The concentration of TiO_2 was approximately 1%. The phantom was also left over night in a hot waterbath with the hope that air bubbles would get more time to rise to the surface and disappear. This did, however, not work as planned. The final phantom still contained a lot of bubbles.

A couple of distance measurements were made on each test phantom and the mean value was put in equation 4.1. The speed of sound was estimated to be 1540 m/s in the candle gel + glass beads phantom as well as in the Agar

+ graphite phantom. The candle gel + TiO_2 phantom had slightly lower speed, 1490 m/s. These results are rough estimates. The errors are large, mostly due to the flaccid consistency of the candle gel making it hard to do measurements with the slide caliper.

Air bubble formation is hard to avoid and presents the biggest challenge. Small bubbles inside a phantom gives strong echo signals, much like echoes from optical fibres, making measurements difficult.

Agar + graphite had acoustic characteristics similar to tissue and is a often used material for ultrasonic phantoms. Its optical features were not similar to tissue, since the graphite made the phantom opaque.

Candle gel + glass beads did not have similar optical features to tissue. The material was practically transparent while tissue is not. The manufacturing process has room for refinements, which hopefully can reduce the number of air bubbles.

The candle gel + TiO_2 phantom had optical features similar to tissue but contained a lot of air bubbles, more than the candle gel + glass beads phantom.

After these initial tests on candle gel, the manufacturing process was modified and a working procedure was established, see appendix C. With this procedure the number of air bubbles were considerably reduced.

At a later point another candle gel + TiO_2 phantom was produced using the new procedure. This time the result had improved. A quick test made with the ultrasound scanner showed, however, that the attenuation was considerably higher than the candle gel + glass beads phantom.

It took a long time to produce the Agar phantoms, the heating took a couple of hours, though the time can be reduced by using a microwave oven. Agar phantoms must be kept moist.

The final choice of material was based on the list outlined in the beginning of this chapter. Main focus was set on the acoustic properties, since the measurements of positions of optical fibres were to be done on ultrasound images. From the initial experiments Agar + graphite and candle gel + glass beads seemed to have similar acoustic properties but candle gel had the big advantage of being reusable. Based on this, candle gel + glass beads was chosen as the primary phantom material.

4.2.2 Acoustic Characteristics of Candle Gel

The three phantoms containing candle gel + glass beads had different concentrations of glass beads. The concentrations were hard to estimate. It

was difficult to get all of the beads out of the glass jar in which the gel was melted. The gel cools down rather quickly, especially close the walls of the jar, and resumes its gelantineous state, thereby encapsulating the beads. The assumption that the concentrations were different was solely based on visual information.

Figure 4.3 shows the signal seen on the oscilloscope for 3 cm and 6 cm pathlength through the phantom material, in this case candle gel + glass beads. Figure 4.4 shows the plot on amplitude (in dB) as a function of frequency and a fitted curve around 5 MHz.

The attenuation measurements for the candle gel + glass beads phantoms were very inconsistent even within the same phantom, inconsistent to the degree that no valuable information could be retrieved. The most probable explanation for this is found in the experimental setup. It was very hard to align the phantoms correctly. The transducers often got in the way and might therefore by mistake have been misaligned. One of the candle gel + glass beads phantoms got a lot of damage when it was removed from the box and could not be used.

The measurements on the pure candle gel phantoms were more successful. All three phantoms could be used for measurements and the results were much more consistent, see table 4.1. The mean value was calculated to $1,44 \pm 0,09\ dB/MHz \cdot cm$. This is valid only at 5 MHz. The attenuation was found not to be linear with frequency.

The reason for that the measurements on the pure candle gel phantoms were more successful than for the candle gel + glass beads phantoms is not fully understood. The measurements on the pure candle gel phantoms were performed a few days after the other phantoms, and after evaluating the result from those, a more careful approach was taken. The pure candle gel phantoms also had a better structure, the surfaces were plane and no air bubbles could be seen. The surfaces of the candle gel + glass beads phantoms were not all plane and there were some air bubbles.

Table 4.1: Attenuation measurements on pure candle gel phantoms

Measurement	*Attenuation* $(dB/MHz \cdot cm)$
1	1,39
2	1,57
3	1,50
4	1,32
5	1,37
6	1,48

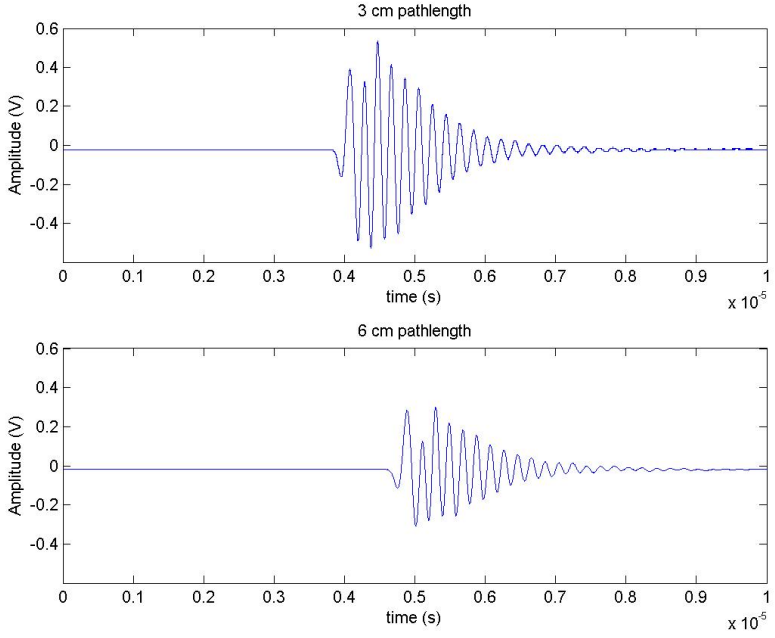

Figure 4.3: The signal seen on the oscilloscope for 3 cm and 6 cm pathlength through the candle gel + glass beads phantom.

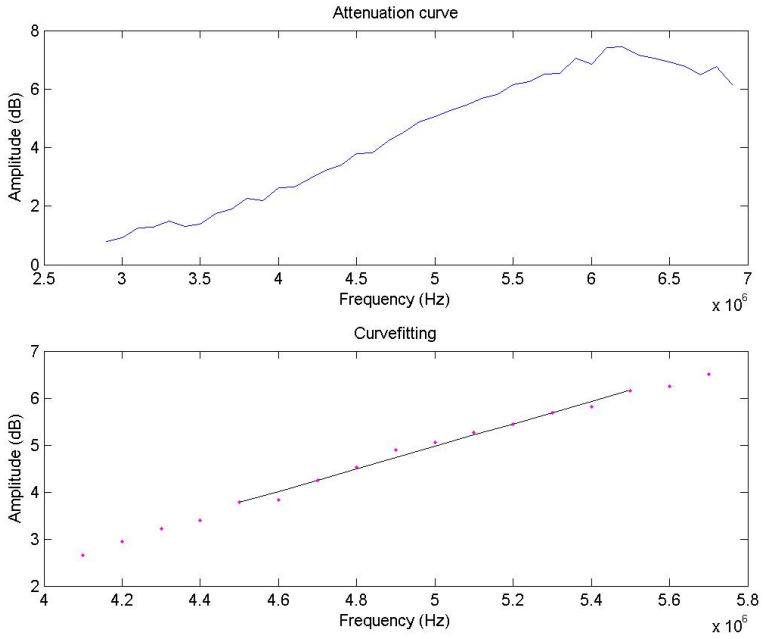

Figure 4.4: Amplitude curve and curvefitting for the candle gel + glass beads phantom.

The speed of sound in the candle gel + glass beads phantom was calculated to 1454 m/s. This speed is lower than the speed measured in prostate tissue. It is also lower than the speed the ultrasound scanner assumes when transforming echo data to images. The difference will cause distances in the direction from the transducer to look larger than they are.

The speed of sound for the candle gel material was lower than first estimated. The speed of sound in prostate tissue is 1561 ± 22 m/s while the speed of sound in the candle gel only was 1454 m/s. The candle gel is in this sense not similar to prostate tissue, but the differing speed of sound can be compensated for. Matching the attenuation of the materials is more important. The candle gel has an attenuation of 1,44 $dB/MHz \cdot cm$ and prostate tissue $0,78 \pm 0,24$ $dB/MHz \cdot cm$. The attenuations does not fully match, but they are of the same order of magnitude.

4.2.3 Optical Characteristics of Candle Gel

Figure 4.5 shows the light distribution over the point of maximum intensity in the image. This point is assumed to be the point directly above the light source, the tip of the optical fiber. The distance from the fiber to the surface was 40 mm. Figure 4.6 shows the logarithmized intensity as a function of distance to the light source. According to equation 4.5 this will be a straight line, and in the figure a fit to a first degree polynomial is shown. From the slope of this curve it is found that $\mu_{eff} = 0,1mm^{-1} = 100m^{-1}$.

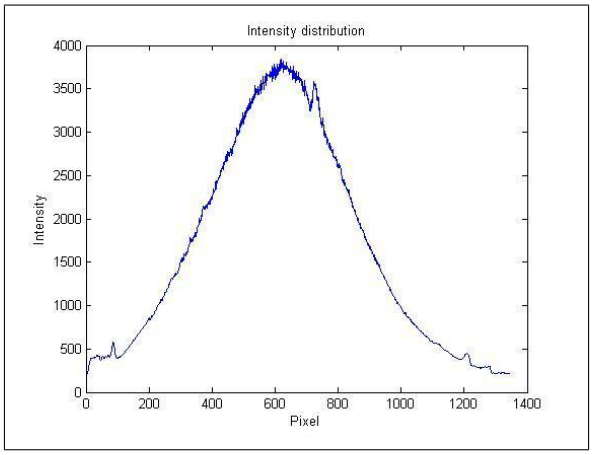

Figure 4.5: Distribution of light intensity in a section across the point right above the light source.

The data generated by the time-resolved system was put in a MatLab program designed for the system and the results can be seen in tables 4.2–4.4. The results were analyzed by an experienced user of the time-resolved sys-

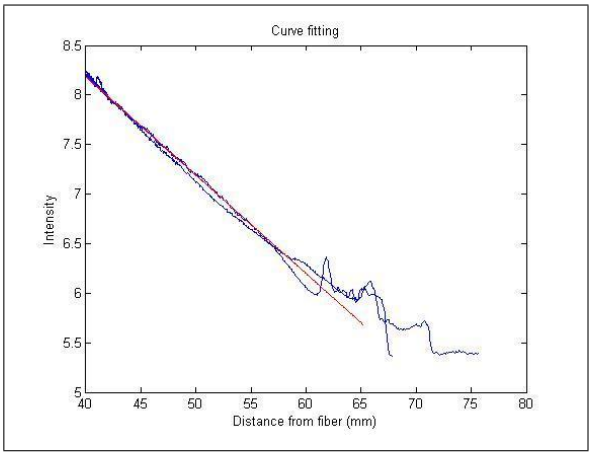

Figure 4.6: The logarithmized intensity as a function of distance from the light source.

tem. For the two longer wavelengths the fitted curves did not fully coincide with the distribution curves and the results from these measurements are therefore not reliable. μ_{eff} was calculated using equation 4.4 and was found to be $\mu_{eff} = 0,391 \pm 0,012cm^{-1} = 39,1 \pm 1,2m^{-1}$.

Table 4.2: Results on μ_s' from the time-resolved measurements.

Distance	$\mu_s'(cm^{-1})$ @ 660 nm	$\mu_s'(cm^{-1})$ @ 785 nm	$\mu_s'(cm^{-1})$ @ 910 nm	$\mu_s'(cm^{-1})$ @ 974 nm
15 mm	5,270	4,483	4,176	4,271
18 mm	5,662	4,800	4,283	4,561
20 mm	5,691	4,572	3,589	3,927

Table 4.3: Results on μ_a from the time-resolved measurements.

Distance	$\mu_a(cm^{-1})$ @ 660 nm	$\mu_a(cm^{-1})$ @ 785 nm	$\mu_a(cm^{-1})$ @ 910 nm	$\mu_a(cm^{-1})$ @ 974 nm
15 mm	0,009	0,011	0,113	0,038
18 mm	0,009	0,011	0,102	0,041
20 mm	0,010	0,011	0,078	0,025

The first method used, where light intensity as a function of distance from light source was studied, gave a higher value for μ_{eff} than the timeresolved method. The question is which method is most reliable. The spatially resolved method had several sources of errors. The surface of the phantom had dust particles on it and was not all smooth. This could be seen on the images taken. The notch seen just beside the peak in figure 4.5 is due to such an

inhomogeneity on the surface of the phantom. The calculations made does not take light reflected at the surface into consideration. The distance from the light source to the surface was measured with a ruler which will introduce a error of approximately 1%. It was also assumed that the point of highest intensity was the point directly above the light source. These errors can be reduced by placing the light source directly on the surface. This setup was tried but did not work due to that the surface of the phantom was not all smooth. Another source of error is reflections against the plexiglas walls of the phantom box. These reflections were not taken in consideration in the calculations. Boundary effects are believed to be the major source of errors.

The time-resolved method also had sources of errors. One of them was air canals in the phantom that were formed when removing brachy needles. The speed of light is different in the canals thereby introducing false arrival times. Light will probably also be reflected due to change in refractive indices. The method measures the optical properties locally and measured values are only valid for the whole phantom if the material is homogeneous. Boundary effects are also a source of error. The largest errors are generated when fitting the theoretical curve to the measurement data. What could seem like a match to an untrained eye could in fact be a quite large mismatch. The almost non-existent absorbation in the phantom was also a problem. The curves for the different wavelengths tended to intrude on each other and the fitting procedure could therefore not use the whole curves. With these sources of errors the absolute value will have an error of at least 10%. The low standard deviation indicates high reproducability.

The time-resolved method uses the diffusion equation while the spatially resolved method uses a simplified version of it. For that reason the time-resolved method is a more reliable method. In these experiments the time-resolved method is also likely to have less errors than the spatially resolved method, mainly due to the boundary effects not considered in the calculations. The spatially resolved method is, however, by far the simplest method and can give a rough estimate.

In a recent study made by Dimtofte et al.[29], μ_{eff} in human prostate tissue was found to vary between 2,5-3,3 cm^{-1}. The phantom produced for the optical measurements had practically no absorption and the scattering was low. It is from an optical view therefore not similar to human prostate tissue, but the optical characteristics can most probably be adjusted with added amount of TiO_2 and a added absorber, for example graphite powder.

Further investigations are needed to establish if candle gel is a good candidate material for phantoms for optical experiments. The big advantage with candle gel would be to have a material that can be used for both optical and acoustic measurements. This reason can make further investigations of suitable concentrations of scatterer and absorber worthwhile.

Table 4.4: Results on μ_{eff} calculated from the time-resolved measurements on μ_a and μ_s.

Distance	$\mu_{eff}(cm^{-1})$ @ 660 nm	$\mu_{eff}(cm^{-1})$ @ 785 nm	$\mu_{eff}(cm^{-1})$ @ 910 nm	$\mu_{eff}(cm^{-1})$ @ 974 nm
15 mm	0,377	0,376	1,205	0,699
18 mm	0,394	0,397	1,159	0,750
20 mm	0,406	0,394	0,927	0,547

Chapter 5

Measurements of Positions

5.1 Image Analysis

Ultrasound images suffer several degrading factors, for example low resolution and speckle. This means that distance information is not easily retrievable, and image analysis has to be used before distances can be measured. A typical ultrasound image of a piece of liver with needles inserted can be seen in figure 5.1. To gather distance information from such an image, the following image analysis methods were used: power-law transformation, extended-maxima transform, opening and fibre location. In each image the lateral direction was denoted x and the axial direction y. The interpolation, extend-maxima transform and opening operations were done with tools available in MatLab R14, while the other operations were constructed for this project. Program code can be found in appendix F.

5.1.1 Power-Law Transformation

A Power-Law transformation is an intensity transformation according to

$$I_{pow} = rI^{\gamma} \tag{5.1}$$

i.e the image intensities taken to some power γ and normalized by r. If $\gamma > 1$ image components with higher intensity are stressed and components with lower intensity are suppressed. Fibre echoes were usually of higher intensity, while speckle generally was of lower intensity. A Power-Law transformation therefore resulted in a contrast improvement between echo objects and speckle. With better contrast it was easier to make accurate objects of the fibre echoes.[30]

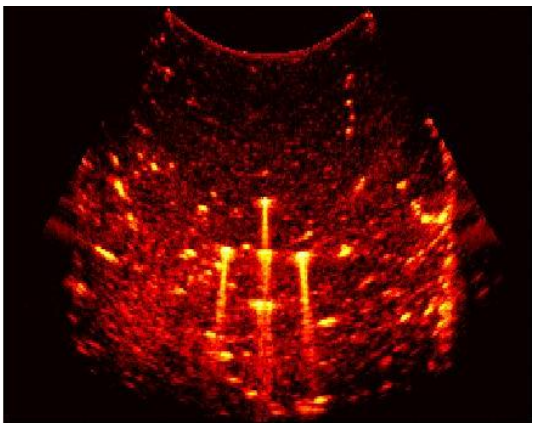

Figure 5.1: A typical ultrasound image of a piece of liver with needles inserted before image processing has been applied. As can be seen it is distorted, making it hard to measure distances directly.

5.1.2 Extended-maxima Transform

The extended-maxima transform is a morphological operation that makes objects out of echoes. Some threshold value is set, and the image is then examined for intensity components higher than this threshold value. The extended-maxima transform thus identified all regional-maxima in an image that were greater than the preset threshold value. Pixels which fulfilled this condition and were connected according to some preset connectivity condition were considered an object. Each object found was then assigned a unique number, a label, that made it possible to distinguish different objects from one another, as well as from the background.[31]

5.1.3 Opening

Opening is a morphological operation that smoothes images. If $A = \{(x, y) \in \mathbb{Z}^2 | f(x, y) = k\}$ is a subset of the image, k is some integer present in the label image and $B \subset \mathbb{Z}^2$ is a structural set, the dilation of A with B is defined as

$$A \oplus B = \{x | ((\hat{B})_x \cap A) \subseteq A\} \tag{5.2}$$

and the erosion of A with B is

$$A \ominus B = \{x | ((\hat{B})_x) \subseteq A\} \tag{5.3}$$

Dilation of A with B expands A with B, and erosion of A with B diminishes (erodes) A with B.

Opening is defined as

$$A \circ B = (A \ominus B) \oplus B \tag{5.4}$$

which means an erosion of A with B followed by a dilation of the result with B. Opening has several properties which are very useful when working with distorted images, namely

- smoothing of outlines.
- removing of narrow passages.
- elimination of small objects.

These properties suppressed features distorting the echoes[30]. Figure 5.2 shows figure 5.1 after image processing.

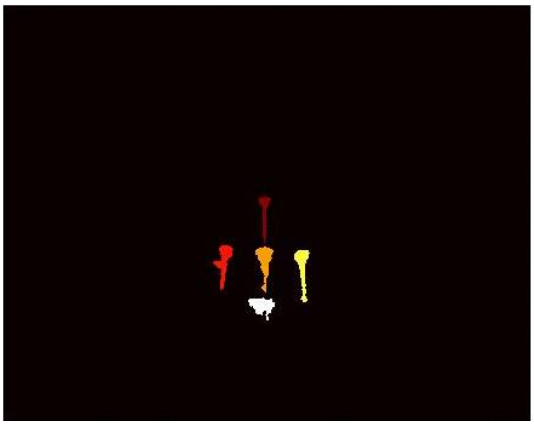

Figure 5.2: Figure 5.1 after after image processing. This is the kind of image which is used to locate the fibre positions. Notice the different colours of the objects. This means that the objects consist of unique numbers (1,2,...) and can therefore easily be distinguished from one another.

5.1.4 Locating the Fibre Position in an Ultrasound Echo

Due to ringing and limited resolution, the echo from a fibre in an ultrasound image is always broadened, making the echo larger than the actual fibre. To obtain accurate fibre positions in the images, it was thus important to calculate where the fibre was in the fibre echo. There were several problems related to this task. For example, grains of speckle could distort the shape of the fibre echo, echoes from fibres close to the transducer could shadow echoes from fibres situated further away.

To solve the problem of finding the position of the fibre inside a fibre echo, three different methods were designed: one using intensity information, one using geometrical information and one fitting a shape to the echo. The fibre positions found by the different methods were later used when calculating distances between fibres.

Intensity

The most obvious choice of method for locating the fibre position in an ultrasound echo, was to use the intensity information in the echo. The intensity in the echo was usually distributed with the maximum intensity situated where the most likely position of the fibre was. It was also a fairly easy method to implement. The maximum intensity/intensities of an echo object in the image was found and the fibre point placed at the most likely position.

The method was very sensitive to shadowing, as can be seen in figure 5.3. When an echo was shadowed by another, the position of maximum intensity differed significantly from the actual position of the fibre. It was, however, not particularly sensitive to speckle distorting the form and size of the object, as long as the speckle was not of high intensity.

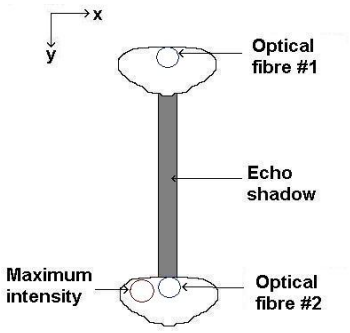

Figure 5.3: The intensity method. Note what happens when the actual fibre position is shadowed by a previous echo.

Geometry

Another approach was to use the geometrical information provided by the echo, i.e. the size and form. The easiest way to do this was to find the spatial extremes of the echo, i.e. the points with the minimum and maximum x coordinates, calculate the average and find the minimum y coordinate for this value, as can be seen in figure 5.4. Since the method is based on the location of a few points, it was sensitive to distortion changing the size and form of the echo object, and also to some extent rotation of the object. Speckle close to a fibre echo expanded the echo object, resulting in an error in the positioning. The method was, however, not sensitive to intensity changes due to echo shadows and such, simply because intensity information was not used at all. This made the location of fibre positions deeper in tissue more accurate than with the intensity method.

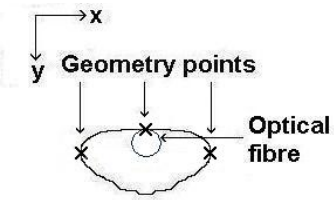

Figure 5.4: The principle behind the geometrical approach. X denotes point used for positioning.

Shape

The third method was to use a shape that represents an undistorted echo object and iteratively fit this to a fibre echo in an ultrasound image. The positioning was then done on the shape instead of the fibre echo. The fitting was done with a combination of translational and rotational operations, trying to maximize the area of the fibre echo covered by the shape. This is called a euclidean transformation, and it is shown in figure 5.5. The transformation can be formulated as:

$$T\begin{bmatrix} x \\ y \end{bmatrix} = \begin{bmatrix} \cos\theta & -\sin\theta \\ \sin\theta & \cos\theta \end{bmatrix} \begin{bmatrix} x \\ y \end{bmatrix} + \begin{bmatrix} t_x \\ t_y \end{bmatrix} \tag{5.5}$$

This approach had several advantages. First, the method was fairly insensitive to distortion in the shape of the fibre echo. This was due to the fact that no operations changing the form of the shape were allowed, only rotation or translation. The method was thus less likely to be effected by speckle-induced distortion. Of course, if there was unfortunately positioned speckle, the method was effected. This problem can to some extent be avoided by the use of speckle reduction techniques. Second, since no intensity information was used, the method was insensitive to shadowing effects altering the position of the maximum intensity or the form of a fibre echo.

The criterion used for determining a fit was the number of points in the shape that covered the fibre echo. An improved fit meant that more points covered the echo.

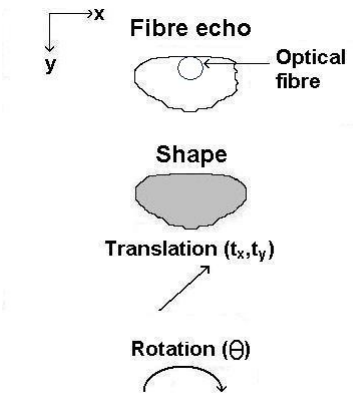

Figure 5.5: The shape method. The operations allowed to fit the shape to a fibre echo are shown.

The approach was as follows:

- Initial Guess

    1. Find the maximum and minimum x coordinates of the echo object and calculate the scaling needed. The distance between x_{min} and x_{max} gave the scaling. To make the method more insensitive to speckle distorting the echo object the scaling was then reduced to 90% of the distance.

    2. Calculate the translation needed. The translation needed was set as the distance between the points (x_{mid},y_{min}) for the shape and (x_{mid},y_{min}) for the echo.

    3. Calculate initial rotation. This was done by calculating the angles between the principal components of the echo object and the x axis.

    4. Update the shape according to the calculated parameters. Initial parameters were denoted T_0.

    5. Set initial step sizes $d\theta$ and dt_x

- Iteration

    1. Determine if a rotation by $\theta \pm d\theta$ and/or a lateral translation by $t_x \pm dt_x$ improves the fit. If so, update θ and/or t_x. Decrease dθ and dt_x.

    2. Determine the axial translation t_y needed to make sure that the point (x_{mid},y_{min}) of the shape is in contact with the echo object.

3. Update the shape according to calculated parameters. These were denoted T_k, where k is the number of iterations.

4. If number of iterations >5 and $\|T_k - T_{k-1}\| \leq \varepsilon$,where ε is some pre-defined tolerance, declare convergence.

One of the weaknesses with this approach was if there was speckle just above the fibre echo distorting the echo object. The shape method then yielded a somewhat non-accurate result. This was an unfortunate side-effect of using the upper part of the boundary of the echo object when determining the axial translation. The method used the upper part of the boundary to ensure that it was not fooled by objects that were elongated in the axial direction. This was often the case when measuring on needles since they tended to ring a lot, thus expanding the echo object axially.

5.2 Methods

The measurements in this project were done on the phantom material, candle gel + glass pearls, and on pieces of beef liver. Two boxes of plexiglass were made, each with the measurements $10 \times 10 \times 10$ cm. On two of the sides, opposite from each other, five holes were drilled in a star pattern and denoted 1-5, as can be seen in figure 5.6. The holes were separated by

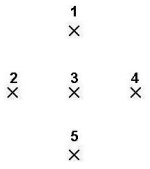

Figure 5.6: The fibre positions and their numbers.

1 cm. The holes were made this way to make it possible to put optical fibres through the box. The holes had a diameter of 0,9 mm (fibre diameter) in one of the boxes and 1,3 mm (needle diameter) in the other, thus making it possible to measure on both fibres and needles. The idea behind this design was that when the actual distances between fibers are known, it is possible to investigate how accurately distance measurements can be done with the ultrasound equipment.

Both phantom and liver measurements were performed with needles and fibres in the boxes. When making the phantom, it was possible to place the fibres before pouring the candle gel in the box. This secured the fibres in both ends and made the distance between the fibres trustworthy all the way through the box. This approach was not possible when measuring on the beef

liver. The optical fibres could not be secured in both ends of the phantom box. Optical fibres bend easily and liver tissue is moderately unyielding, making use of rigid needles a necessity. The fibres were then placed in the tissue through the needles. This meant that only distances close to the side where the needles were inserted could be trusted, where the deflection could be considered sufficiently small.

The measurements were done with a curvilinear transducer and a US scanner. The curvilinear transducer was kept in place with a holder. Separate cross section images as well as cross section movies were stored. Some of the movies were recorded with the purpose of testing ideas regarding image enhancement.

One of the difficulties when recording cross section images was speckle distortion resulting in a reduced image quality. To avoid this problem, a summation of uncorrelated images was evaluated. When the transducer was moved across the sample, the speckle pattern changed while the fibre did not. This meant that it was possible to record cross section images close together and average, reducing speckle in the process.

Measuring on liver presented additional difficulties in the form of strong echoes from fat particles in the tissue. These looked very much like fibres and thus made it hard to determine what was fibre and what was fat. To distinguish between fibres and fat, movies were recorded where a fibre was inserted and then removed. These were used to test if the specificity regarding fibre detection could be increased.

The cross section images and movies were studied using several image analysis methods. The approach was as follows:

1. Interpolate the images using bicubic interpolation. Bicubic interpolation means interpolation by cubic splines. This gives the ability to, in some sense, do sub pixel detection. This is a necessary step, since the resolution of the original pictures is low, usually 0,4 mm/pixel. Bicubic interpolation is somewhat slow but generally gives good results.[30]

2. Power-Law Transformation, in order to get better contrast between fibre echoes and speckle of lower intensity.

3. Extended-maxima transform, to make objects of the echoes.

4. Opening, which reduces distortion to the echo objects.

5. Location of fibre positions in the relevant echo objects. The relevant echo objects were chosen by hand.

All possible distances between fibres were then measured, i.e. the distances between 1-2, 1-3 and so on, making a total of 10 axial and 10 lateral distance

measurements for each cross section. The 10 distances consisted of 3 of approximately 0 mm, 6 of 10 mm and 1 of 20 mm.

In addition to the phantom and liver cross section images, several cross section images of prostate from a brachytherapy session were acquired. These were used to see if the developed approach for fibre positioning only worked for the materials studied in this project or if it could be used for clinical images of prostate as well.

5.3 Results and Discussion

5.3.1 Location of Fibres

Figure 5.7 shows the different position algorithms on an echo from a phantom measurement. The intensity method gives a position that is a bit off in the axial direction. The geometry and shape methods both present a likely position.

Figure 5.8 shows the different position algorithms on an echo from a different phantom measurement. The geometry method gives a position that is a bit off both in the axial and lateral direction, probably due to speckle distorting the echo shape on the left side. The intensity and shape method both present a likely position.

Figure 5.9 shows the different position algorithms on an echo from a liver measurement. The geometry method gives the most likely position of the three. The echo is very distorted from shadowing and speckle. Shadowing from another echo effects the intensity method and speckle just above the echo effects the shape method. Due to symmetrical speckle in the lateral direction, the geometry method is not as effected by the distortion as the other methods. This image represents a worst case scenario.

Figure 5.10 shows the different position algorithms on two echoes from a different liver measurement. There is a lot of ringing from the needles inserted, but it does not effect any of the methods. The intensity method gives a position that is a bit off in the axial direction, especially for the left object. The geometry method gives a likely result. The right object is marginally off in the axial direction. The shape method gives a likely result.

The intensity method is sensitive to intensity distortions. The greater the distance the greater the likelihood is that distorting events have occurred and therefore a poorer result with increasing distance from transducer will be seen.

The geometry method gives good results in the images shown, but it is

sensitive to rotation of objects and speckle. A larger set of images will not give such a good result.

Generally the shape method gives a likely position for the fibres. The method uses the relation between a large set of points, whereas the two other methods use only a few points. This makes the shape method more insensitive to form and intensity distortions.

The fibre positioning programme, which performs the three positioning algorithms, takes about 2 minutes to run per image. The interpolation part has the largest time complexity. The computer used was a Intel Pentium II 451 MHz with 256 MB RAM.

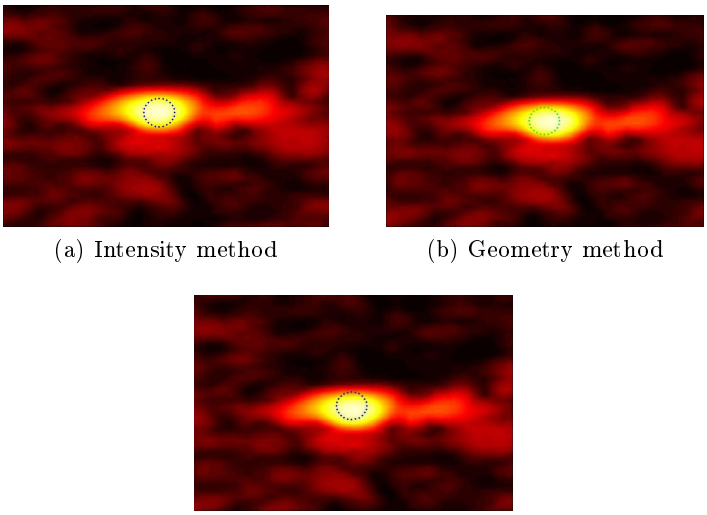

(a) Intensity method (b) Geometry method

(c) Shape method

Figure 5.7: Applied fiber position algorithms on a phantom US image.

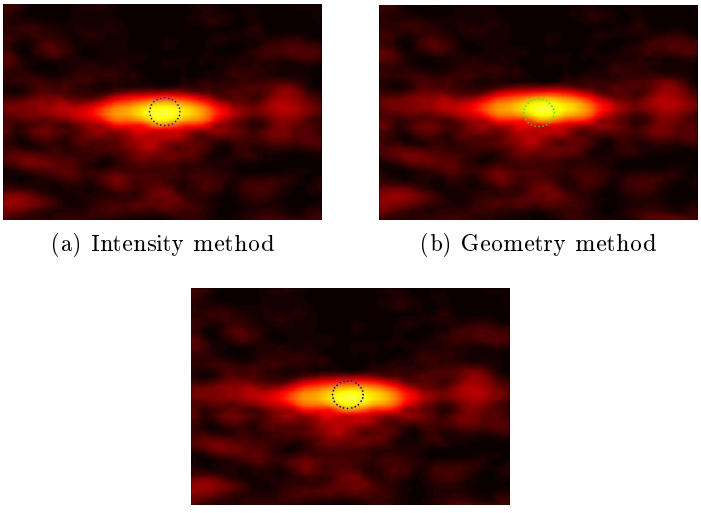

(a) Intensity method (b) Geometry method

(c) Shape method

Figure 5.8: Applied fiber position algorithms on another phantom US image.

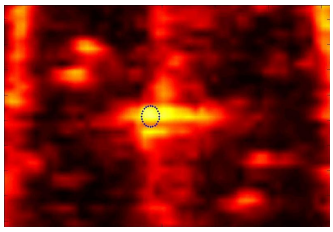

(a) Intensity method

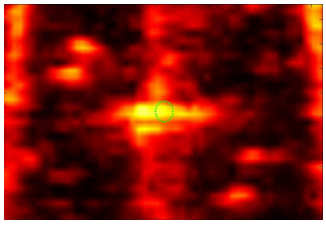

(b) Geometry method

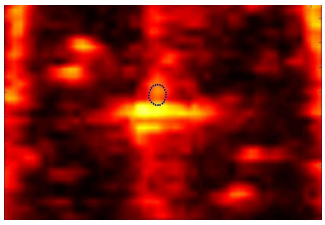

(c) Shape method

Figure 5.9: Applied fiber position algorithms on a liver US image.

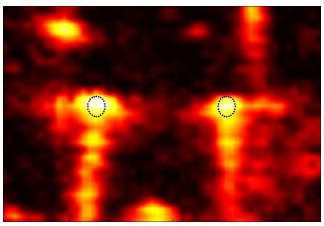

(a) Intensity method

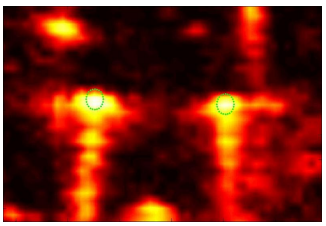

(b) Geometry method

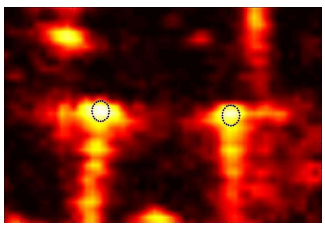

(c) Shape method

Figure 5.10: Applied fiber position algorithms on another liver US image.

5.3.2 Distance Measurements

Phantom Measurements

Figures can be found in appendix A. Figures A.1–A.6 each show four sets of data. They contain 10, 10, 7 and 10 images respectively. In the phantom both needles and fibres were inserted. For axial measurements a correction in speed of sound was made by multiplying the distance with the fraction of the assumed speed of sound and the real speed of sound. An assumption was made that the angles of the sound emitted and received by the transducer was small.

Figure A.1 shows distance measurements at 0 mm laterally for the different methods. The mean value is generally a bit too high. The overall standard deviation for the different methods is approximately the same.

Figure A.2 shows distance measurements at 10 mm laterally for the different methods. The correct distance is within the error margins for all three methods. The mean values for the shape method is closer to correct value than the other methods.

Figure A.3 shows distance measurements at 20 mm laterally for the different methods. All the mean values are a bit too high. Compared to the measurements at 10 mm, the error in mean value is generally twice as large. This implies a systematic error. The standard deviation is smallest for the shape method.

Figure A.4 shows distance measurements at 0 mm axially for the different methods. All mean values are about the same, and a bit too high. The standard deviation is approximately the same for the different methods.

Figure A.5 shows distance measurements at 10 mm axially for the different methods. The compensated correct value is within the error margins for all three methods. The standard deviation is about the same for all methods and quite large.

Figure A.6 shows distance measurements at 20 mm axially for the different methods. The mean values are a bit too low compared to the compensated correct value. The standard deviations are generally small.

Table 5.1 shows the average mean value for the different methods at the different distances. The standard deviations are generally small, less than 0,5 mm. When considering deviation from correct value the shape method gives the best result, excluding the 10 mm and 20 mm axial measurements. Table 5.2 shows the 10 mm and 20 mm axial measurements compensated for differing speed of sound. The correction was made by multiplying the values with the fraction of the real speed of sound and the assumed speed of

sound. As can be seen the values for the different methods are all close to the compensated value.

The mean values in both axial and lateral direction, for all distances, are too high. This could be due to sound speed components not only in the axial direction but also in the lateral direction. Both depend on the design of the transducer, see figure 5.11. Errors can also be found in the experimental setup: the fibres and needles may have been slightly deflected, the transducer may have been tilted and the distances between the holes in the box may not be as exact as assumed. These error sources can be a cause for the systematic errors seen.

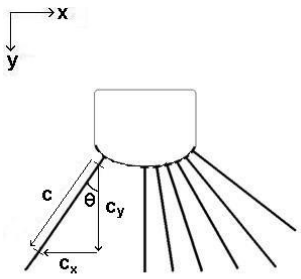

Figure 5.11: Sound emitted from a curvilinear transducer.

The measurements of distances in lateral direction is closer to the correct value than in the axial direction. With correction for differing speed of sound in the axial direction the values are very close to the desired result. The reason for the errors not being as large in the lateral direction as in the axial is not fully understood but might be due to that many transducer elements are used when emitting and receiving.

Liver Measurements

Figures can be found in appendix A. Figures A.7–A.12 each show four sets of data. They contain 7, 9, 10 and 10 images respectively. In the phantom both needles and fibres were inserted. For axial measurements a correction in speed of sound was made by multiplying the distance with the fraction of the assumed speed of sound and the real speed of sound. An assumption was made that the angles of the sound emitted and received by the transducer was small.

Figure A.7 shows distance measurements at 0 mm laterally for the different methods. The mean values are generally quite high, with large standard deviations.

Figure A.8 shows distance measurements at 10 mm laterally for the different methods. The correct value is within the error margins for all three methods, but the standard deviations are quite large.

Figure A.9 shows distance measurements at 20 mm laterally for the different methods. The correct value is within the error margins for the geometry method. This method has, however, the largest standard deviation. The intensity method diverges the most from correct value. Compared to the measurements at 10 mm, the error in mean value is generally twice as large. This implies a systematic error.

Figure A.10 shows distance measurements at 0 mm axially for the different methods. The mean values for all the methods are quite high. The geometry method has a very large standard deviation. The intensity and shape methods have similar mean values and standard deviations.

Figure A.11 shows distance measurements at 10 mm axially for the different methods. The compensated correct value is within the error margins for all methods. The standard deviations are quite large, especially for the geometry method. For data sets 2 and 3, the shape method gives a lower mean value than the two other.

Figure A.12 shows distance measurements at 20 mm axially for the different methods. The intensity method shows the best behavior with respect to mean value and standard deviation. The geometry method shows similar results, but its error margins does not overlap the compensated correct value for all data sets. The lower mean value for the shape method is also seen here.

Table 5.3 shows the average mean values for the different methods at the different distances. The standard deviations are larger than for the phantom measurements, in lateral direction generally over 0,5 mm. When considering deviation from correct value the shape method gives the best result, exclud-

ing the 10 mm and 20 mm axial measurements. Table 5.4 shows the 10 mm and 20 mm axial measurements compensated for differing speed of sound. The correction was made by multiplying the values with the fraction of the real speed of sound and the assumed speed of sound. As can be seen the values for the different methods are all close to the compensated value.

The mean values for the 0 mm distance are too high in both the axial and lateral directions. The unyielding nature of the liver made it difficult to keep the needles and fibres straight all the way through the box. It was also hard to estimate any deflection, due to the opacity of the material. Some errors can probably also be found in the experimental setup, mainly tilting of the transducer and accuracy of holes in the box. These error sources can be a cause for the systematic errors seen.

Values in the lateral direction were close to correct value. The differences are smaller than for corresponding phantom measurements. The assumed speed of sound in the ultrasound scanner is closer to the speed of sound in liver tissue than in the phantom material. This is probably the explanation for the smaller differences.

With correction for differing speed of sound in the axial direction the values are very close to the desired result, at least for the intensity and geometry methods.

For data sets 2 and 3, the shape method gives a lower mean value than the two other methods. The second data set is known to have several images with highly distorted echo objects, see for example figure 5.9. These distortions seem to effect the shape method more. The axial translation calculations are sensitive to speckle distortion just above the object. The geometry method should also have been effected, but due to that the speckle distortion was not placed in the center above the object, it was not.

Table 5.1: Average mean values with average standard deviation for the different methods for different distances in phantom.

Measurement/Method	*Intensity (mm)*	*Geometry (mm)*	*Shape (mm)*
x0	$0,46 \pm 0,25$	$0,45 \pm 0,28$	$0,42 \pm 0,25$
x10	$10,26 \pm 0,41$	$10,25 \pm 0,39$	$10,16 \pm 0,34$
x20	$20,53 \pm 0,30$	$20,49 \pm 0,25$	$20,31 \pm 0,13$
y0	$0,51 \pm 0,30$	$0,58 \pm 0,31$	$0,52 \pm 0,30$
y10	$10,51 \pm 0,46$	$10,59 \pm 0,49$	$10,561 \pm 0,44$
y20	$21,02 \pm 0,17$	$21,19 \pm 0,18$	$21,12 \pm 0,14$

Table 5.2: Average mean values with average standard deviation for the different methods for different distances in phantom with correction for deviation in speed of sound.

Measurement/Method	*Intensity (mm)*	*Geometry (mm)*	*Shape(mm)*
y10	$9,93 \pm 0,46$	$10,00 \pm 0,49$	$9,97 \pm 0,44$
y20	$19,85 \pm 0,17$	$20,00 \pm 0,18$	$19,94 \pm 0,14$

Table 5.3: Average mean values with average standard deviation for the different methods for different distances in liver.

Measurement/Method	*Intensity (mm)*	*Geometry (mm)*	*Shape (mm)*
x0	$1,03 \pm 0,53$	$0,87 \pm 0,63$	$0,92 \pm 0,60$
x10	$9,83 \pm 0,84$	$9,98 \pm 0,72$	$9,91 \pm 0,73$
x20	$19,65 \pm 0,16$	$19,96 \pm 0,35$	$19,82 \pm 0,18$
y0	$0,62 \pm 0,40$	$0,77 \pm 0,68$	$0,57 \pm 0,27$
y10	$9,73 \pm 0,47$	$9,76 \pm 0,72$	$9,59 \pm 0,48$
y20	$19,46 \pm 0,24$	$19,50 \pm 0,19$	$19,18 \pm 0,30$

Table 5.4: Average mean values with average standard deviation for the different methods for different distances in phantom with correction for deviation in speed of sound.

Measurement/Method	*Intensity (mm)*	*Geometry (mm)*	*Shape (mm)*
y10	$10,04 \pm 0,47$	$10,07 \pm 0,72$	$9,89 \pm 0,48$
y20	$20,08 \pm 0,24$	$20,12 \pm 0,19$	$19,79 \pm 0,30$

Conclusions on Phantom and Liver Distance Measurements

The intensity method was the simplest method tested, but gave surprisingly good results. The method is very sensitive to intensity distorting factors, for example shadowing. Shadowing is the dominating source of error.

In the liver measurements the geometry method had large standard deviations. In the phantom measurements they were comparable to the standard deviations of the other two methods. As stated before the geometry method is a simple method and it is sensitive to many factors, especially to tilting. It is not as sensitive to symmetrical distortions as to asymmetrical distortions.

The shape method is good but not flawless. The shape method was designed to be as stable and robust as possible and to work in many measurement situations. The design makes the method the best of the three methods tested. Some refinements can be made.

The fibres in the phantom measurements were most likely a bit deflected, maximum 1 mm at the center of the box. There was no obvious deflection to the naked eye. The accuracy of the holes in the box was approximately $\pm$0,1 mm, introducing an error of about 1%.

The resolution of the ultrasound transducer also needs to be considered. The mean frequency is approximately 4 MHz which translates to a cycle period time of 0,25 μs. An average pulse is about 2 cycles, resulting in a pulse length of 0,5 μs. This gives an axial resolution of 0,8 mm. This means that two objects can not be closer than 0,8 mm. Lateral resolution depends on the distance to focus point. In the focus point the resolution is approximately 0,7 mm. These numbers are based on a qualified estimation. This will not effect the positioning as long as the objects are further apart than the resolution. The most important factor for the positioning is the pixel size.

The image enhancing techniques evaluated, summation of uncorrelated images and needle movement, did not result in any improvements. This could be due to:

- a lot of fat particles in the liver samples making the images hard to interpret.
- air channels both in the liver tissue and in the phantom material giving false responses.
- the transducer not being aligned the same way in consecutive images.

5.3.3 Tests on Clinical Images

The result of the image analysis procedure, presented in section 5.1.4, is shown in figure 5.12. The fibres visible in the original image are also seen in the object image.

Figure 5.13 shows the fibre position algorithms applied on one of the fibres. The geometry and shape methods gave a plausible location of the fibres. This means that the fibre position methods should work in clinical cases as well.

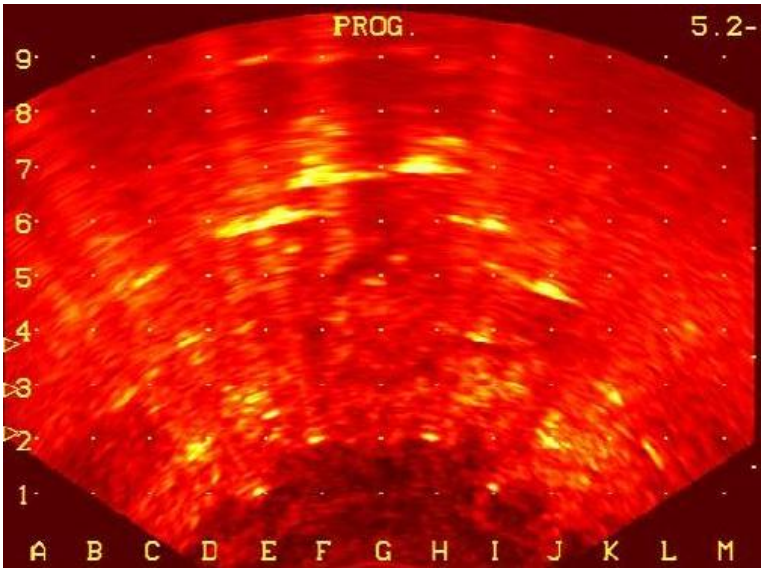

(a) Original image

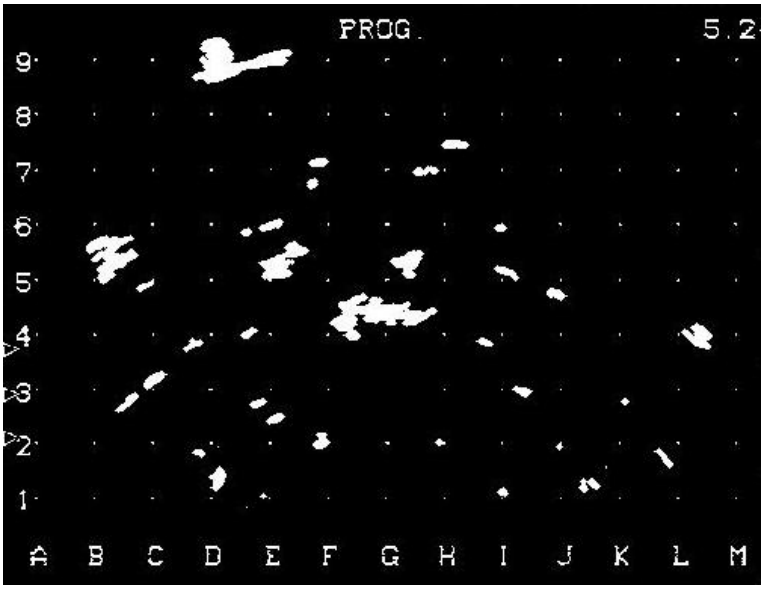

(b) Extended maxima transform

Figure 5.12: Applied image analysis on clinical images.

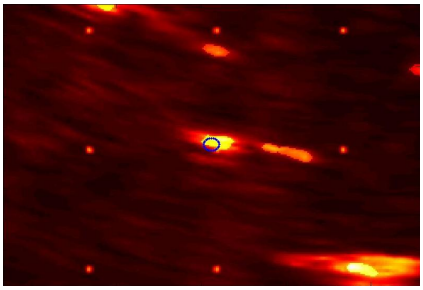

(a) Intensity method

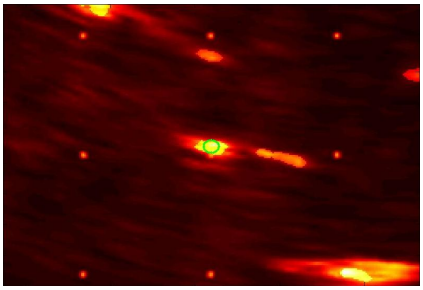

(b) Geometry method

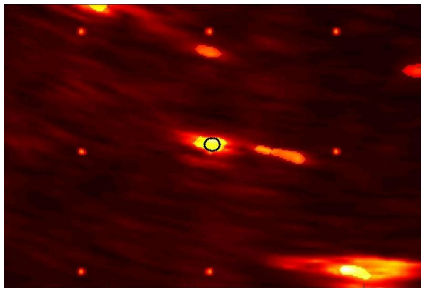

(c) Shape method

Figure 5.13: Applied fiber position algorithms on a US image from brachytherapy.

Chapter 6

Summary and Conclusions

The experimental work in this thesis can be divided into two major parts. Finding and evaluating a tissue equivalent material and distance measurements.

6.1 Summary

6.1.1 The Phantom

Two different base materials, candle gel and Agar, with different additives were tested. After preliminary tests candle gel with glass pearls was chosen as the most suitable material for this project. The candle gel was further analyzed and characterized both acoustically and optically. The speed of sound was estimated to 1454 m/s and the attenuation to $1,44 \pm 0,09\ dB/MHz \cdot cm$.

The effective attenuation, μ_{eff}, was estimated to $39,087 \pm 1,191\ m^{-1}$ with the time-resolved method and 100 m^{-1} with the spatially resolved method.

6.1.2 Distance Measurements

Distance measurements were done on needles and optical fibres inserted in the phantom material as well as in a piece of beef liver. The distance measurements were done on ultrasound images using three different fibre position algorithms, an intensity method, a geometry method and a shape method. The distances evaluated were 0, 10 and 20 mm laterally and axially.

In the phantom material, with the intensity method, the deviation to correct value was on average 0,42 mm laterally and 0,24 mm axially and the standard deviation averaged 0,31 mm in the lateral direction and 0,31 mm in the axial

direction. A compensation in axial direction was made for deviating speed of sound between actual speed in the material and assumed speed in the ultrasound scanner.

With the geometry method the deviation to correct value was on average 0,39 mm laterally and 0,19 mm axially and the standard deviation averaged 0,31 mm in the lateral direction and 0,32 mm in the axial direction. Measurements in axial direction were compensated for deviating speed of sound.

With the shape method the deviation to correct value was on average 0,25 mm laterally and 0,20 mm axially and the standard deviation averaged 0,24 mm in the lateral direction and 0,29 in the axial direction. Measurements in axial direction were compensated for deviating speed of sound.

In the liver material, with the intensity method, the deviation to correct value was on average 0,52 mm laterally and 0,24 mm axially and the standard deviation averaged 0,51 mm in the lateral direction and 0,37 mm in the axial direction. A compensation in axial direction was made for deviating speed of sound.

With the geometry method the deviation to correct value was on average 0,32 mm laterally and 0,19 mm axially and the standard deviation averaged 0,56 mm in the lateral direction and 0,53 mm in the axial direction. Measurements in axial direction were compensated for deviating speed of sound.

With the shape method the deviation to correct value was on average 0,40 mm laterally and 0,30 mm axially and the standard deviation averaged 0,50 mm in the lateral direction and 0,35 mm in the axial direction. Measurements in axial direction were compensated for deviating speed of sound.

6.2 Conclusions

The goal was to see how accurately the positions of optical fibres in tissue can be determined with ultrasound. The deviation from correct value was generally less than 0,5 mm. The standard deviation for the shape method, the most stable method, was approximately 0,3 mm in the phantom measurements and slightly higher in the liver measurements. This will result in a span of 0,6 mm around the mean value. In a worst case scenario this means a deviation from correct value of less than a millimeter. This is also valid for the liver measurements.

The work has shown that it is possible to find fibre positions with high accuracy with ultrasound, and we believe that SpectraCure AB will benefit from our results.

The chosen phantom material had its pros and cons. The material was reusable, a major advantage, and it was easy to work with. However, its acoustic properties were not as similar to prostate tissue as first anticipated. The differing speed of sound could be corrected for.

The positioning programme took about 2 minutes to run. This is an acceptable time and the programme can most likely be optimized further.

6.3 Future work

The shape algorithm has room for some improvements to further enhance the stability and efficiency.

One of the problems with the shape algorithm as it is presently implemented, is that it only uses the point (x_{mid},y_{min}) of the shape when calculating the axial translation. If there is speckle situated above the fibre echo, the axial translation will be off. One way to solve this problem is to use not just the point (x_{mid},y_{min}), but additional points situated on equal distances from this midpoint and set some threshold as for how many of these points should be in contact with the boundary of the echo object.

Scaling is not used in the shape algorithm, apart from the initial scaling. If full scaling is allowed, making the euclidean transformation a similarity transformation, the specificity of the algorithm should be improved.

The ultrasound scanner used in the clinic, BK-Medical Falcon 2101, does not have any built in speckle reduction features. All images in this thesis work were recorded without using any speckle reduction techniques. Images will most likely improve with such features.

Images recorded both in clinic and in this thesis work were extracted from the video signal of the scanner. The video signal contains less information than the raw image data and valuable data will be lost in the transfer process. It would be useful to have direct connection between the raw image data and the data evaluation programme. This requires both hardware and software interfaces. The system used today for brachytherapy uses the video signal.

With further optimization of the algorithms and adjustments to the software available at treatment site, we believe that the work done can be implemented in the clinical application. This implementation is subject for future work.

At present the fibres are marked by hand. This is a difficult and tedious task when dealing with many fibres. An automatic procedure is therefore favorable. The shape method could be used as a template to distinguish between fibre echoes and other echoes. From the dose plan it is known

where the fibres should be. This information can be used to establish a search pattern.

The chosen phantom material, candle gel, can be further analyzed for optical applications. The material might also have other uses not investigated here, for example in magnetic resonance measurements.

Acknowledgements

First of all we would like to thank our supervisors and sub-supervisors, there was a bunch. Professor Stefan Andersson-Engels, Ann Johansson, Johan Axelsson at Atomic Physics, Monica Almquist and Tomas Jansson at Electric Measurements and Thomas Johansson and Johan Stensson at SpectraCure AB. There has always been someone to ask...

We would also like to thank, in no particular order:

Dr. Margrèt Einarsdòttir for letting us visit a brachytherapy session and being patient with our endless questions.

Peter Jonsson for helping us with measurements of acoustic properties.

Johan Karlsson for helping us with image analysis.

Anders Nilsson and Jimmy Lett for taking time to take magnetic resonance images of our phantoms.

Tomas Svensson for helping us with the time-resolved spectroscopy measurements.

Christoffer Abrahamsson for reading, and correcting, parts of our report and helping us with the spatially resolved measurements.

and everyone at Electric Measurements with a key...

Bibliography

1. A. Tallberg. *Prostata: Mannens problemkörtel.* Wahlström och Widstrand, Stockholm, 1960.

2. K.L Moore and A.M.R Agur. *Essential clinical anatomy.* Lippincott, Williams and Wilkins, Baltimore, 1995.

3. J.W. Rohen and B. Sandström. *Topografisk Anatomi.* Bokförlaget Natur och Kultur, Stockholm, 1975.

4. *Vårdprogram prostatacancer (2004).* www.ocsyd.lu.se /Vardprog/Prostatacancer%202004.pdf [8 Nov 2005].

5. S. Nilsson, R. Henriksson, L. Andersson, U. Ringborg, R. Henriksson, and S. Friberg. *Onkologi*, chapter Urologisk cancer, pages 268–273. Liber AB, Stockholm, 1998.

6. *The Prostate cancer infolink. Understanding Gleason Grading.* www.phoenix5.org/Infolink/GleasonGrading.html [11 Nov 2005].

7. D.F. Gleason and M. Tannenbaum. *Urologic Pathology: The Prostate*, chapter The Veteran's Administration Cooperative Urologic Research Group: Histologic grading and clinical staging of prostatic carcinoma, pages 171–198. Lea and Febiger, Philadephia, 1977.

8. International Union Against Cancer (UICC), L.H. Sobin, and C.H. Wittekind. *TNM Classification of malignant tumours.* Wiley-Liss, New York, 6th edition, 2002.

9. *Treatment options.* www.nyprostate.org/treatment_options.cfm [6 Dec 2005].

10. M. Soto Thompson. *Photodynamic therap utilizing interstitial light delivery combined with spectroscopy methods.* PhD thesis, 2004.

11. J.-L. Boulnois. Photophysical processes in recent medical laser developments: a review. *Lasers in Medical Science*, 1:47–66, 1986.

12. S.A. Prahl. Tabulated molar extinction coefficient for hemoglobin in water, 1998.

13. J.R. Mourant, T.M. Johnson, V. Doddi, and J.P. Freyer. Angular dependent light scattering from multicellular spheroids. *Journal of Biomedical Optics*, 7(1):93–99, 2002.

14. B. Beauvoit, S.M. Evans, T.W. Jenkins, E.E. Miller, and B. Chance. Correlation between the light scattering and the mitochondrial content of normal tissues and transplantable rodent tumors. *Analytical Biochemistry*, 226(1):167–174, 1995.

15. C. af Klinteberg. *On the use of light for the characterization and treatment of malignant tumours*. PhD thesis, Lund, Sweden, 1999.

16. M.R. Arnfield, J. Tulip, and M.S. McPhee. Optical propagation in tissue with anisotropic scattering. *IEEE Transactions on Biomedical Engineering*, 35(5):372–381, 1988.

17. W.-F. Cheong, S.A. Prahl, and A.J. Welch. A review of the optical properties of biological tissues. *IEEE Journal of Quantum Electronics*, 26(12):2166–2185, 1990.

18. C. Abrahamsson. *Time-resolved spectroscopy for pharmaceutical applications*. PhD thesis, 2005.

19. K.R. Weishaupt, C.J. Gomer, and T.J. Dougherty. Identification of singlet oxygen as the cytotoxic agent in photo-inactivation of a murine tumor. *Cancer Research*, 36(7):2326–2329, 1976.

20. F. Stewart, P. Baas, and W. Star. What does photodynamic therapy have to offer radiation oncologists (or their cancer patients)? *Radiothermal Oncology*, 48:233–248, 1998.

21. S.B. Brown, E.A. Brown, and I. Walker. The present and future role of photodynamic therapy in cancer treatment. *Lancet Oncology*, 5(8):497–508, 2004.

22. N.E Martin and S.M. Hahn. Interstitial photodynamic therapy for prostate cancer: a developing modality. *Photodiagnosis and Photodynamic Therapy*, 1(2):123–136, 2004.

23. M. Soumaya and T.H. Foster. Carbogen breathing significantly enhances the penetration of red light in murine tumours in vivo. *Physics in Medicine and Biology*, 49(10):1891–1904, 2004.

24. R.A. Weersink, A. Bogaards, M. Gertner, S.R.H. Davidson, K. Zhang, G. Netchev, J. Trachtenberg, and B.C. Wilson. Techniques for delivery and monitoring of tookad (wst09)-mediated photodynamic therapy of the prostate: Clinical experience and practicalities. *Journal of Photochemistry and Photobiology B-Biology*, 79(3):211–222, 2005.

25. P. Fish. *Physics and instrumentation of diagnostic medical ultrasound.* John Wiley and Sons Ltd., Chichester, 1990.

26. J.A Zagzebski. *Essentials of Ultrasound physics.* CV Mosby, London, 1996.

27. J.C. Bamber and C.R. Hill. Ultrasonic attenuation and propagation speed in mammalian organs as a function of temperature. *Ultrasound Med.Biol.*, 5(2):149–157, 1979.

28. K.J Parker, S.R Huang, R.M Lerner, F. Lee Jr, D. Rubens, and D. Roach. Elastic and ultrasonic properties of the prostate 1993 ultrasonic symposium. 1993.

29. A. Dimofte, J.C. Finlay, and T.C. Zhu. A method for determination of the absorption and scattering properties interstitially in turbid media. *Physics in Medicine and Biology*, 50(10):2291–2311, 2005.

30. R.C. Gonzales and R.E. Woods. *Digital image Processing.* Prentice Hall, Upper Saddle River, N.J., 2nd edition, 2002.

31. P. Soille. *Morphological Image Analysis: Principals and Applications.* Springer-Verlag, Heidelberg, 1999.

32. L. Jäger, G.U. Müller-Lisse, R. Gutmann, J. Feyh, M. Thoma, and M. Reiser. Erste ergebnisse der mrt-gesteuerten laserinduzierten interstitiellen thermotherapie von kopf- und halstumoren. *Der Radiologe*, 36(3):236–244, 1996.

33. G.U. Müller-Lisse, A. Heuck, M.K. Stehling, M. Frimberger, M. Thoma, P. Schneede, R. Muschter, A. Hofstetter, and M. Reiser. Mrt-monitoring vor, wahrend und nach der interstitiellen laserinduzierten thermotherapie der benignen prostatahyperplasie -erste klinische erfahrungen. *Der Radiologe*, 36(9):722–731, 1996.

Appendix A

Figures

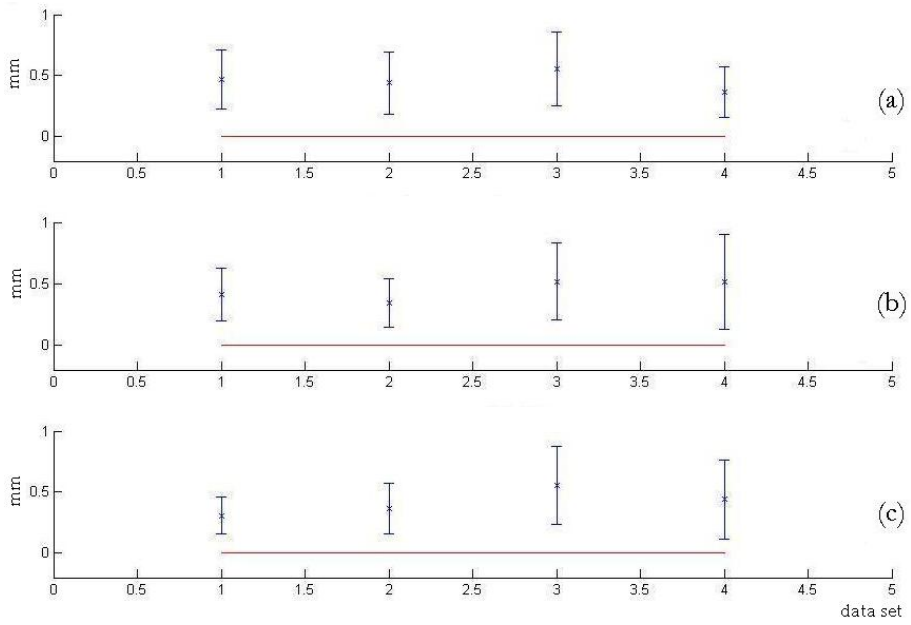

Figure A.1: Measurements at 0 mm laterally in phantom. (a) Intensity method. (b) Geometry method. (c) Shape method. Solid line represents correct value.

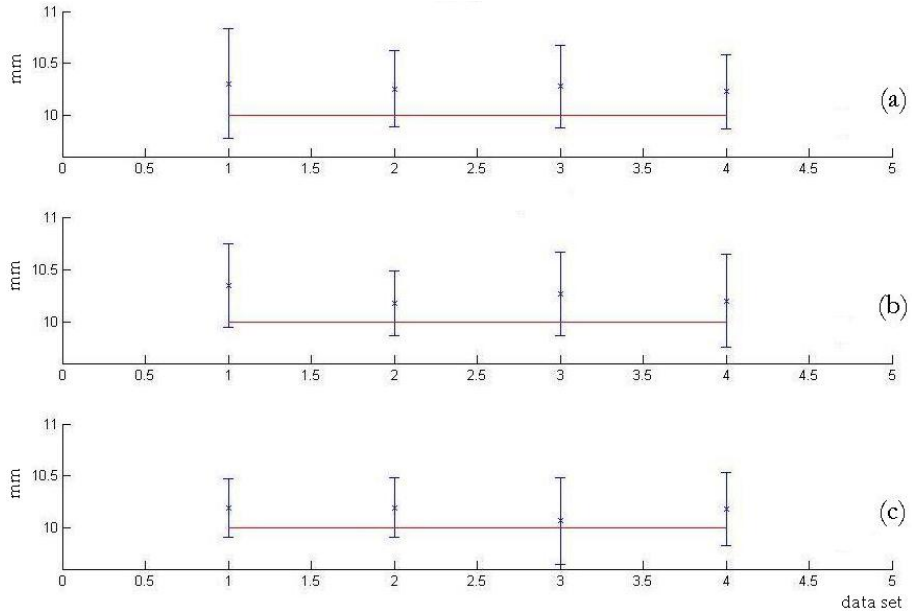

Figure A.2: Measurements at 10 mm laterally in phantom. (a) Intensity method. (b) Geometry method. (c) Shape method. Solid line represents correct value.

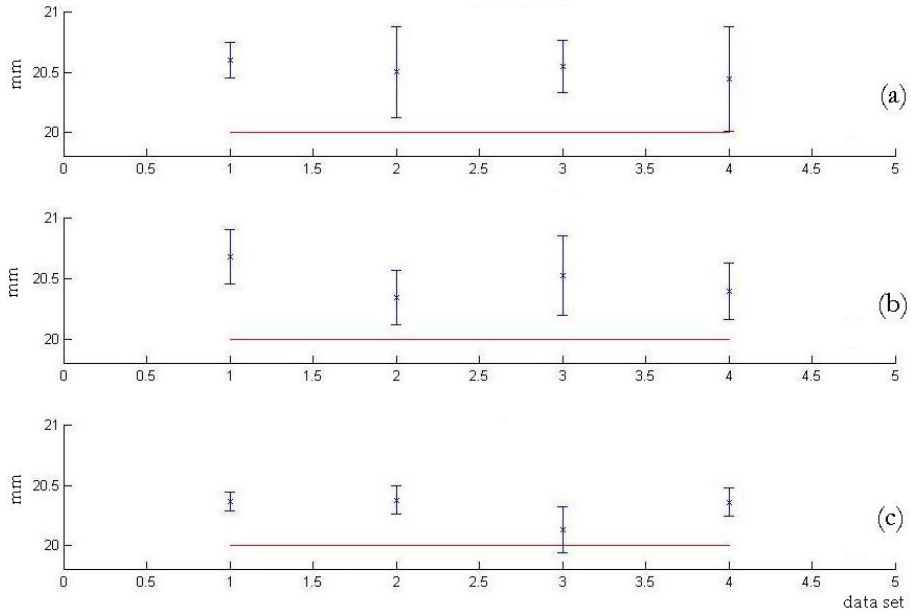

Figure A.3: Measurements at 20 mm laterally in phantom. (a) Intensity method. (b) Geometry method. (c) Shape method. Solid line represents correct value.

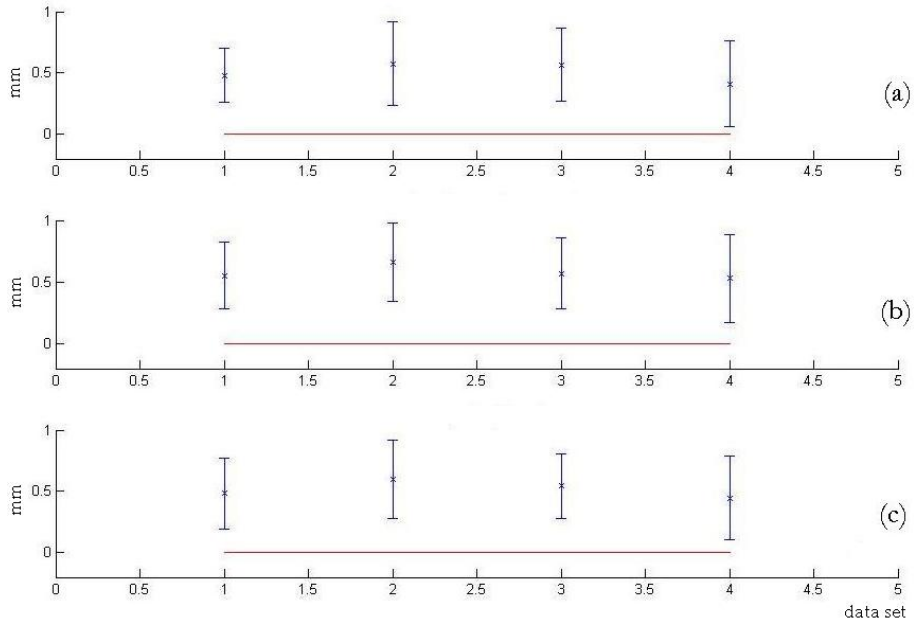

Figure A.4: Measurements at 0 mm axially in phantom. (a) Intensity method. (b) Geometry method. (c) Shape method. Solid line represents correct value.

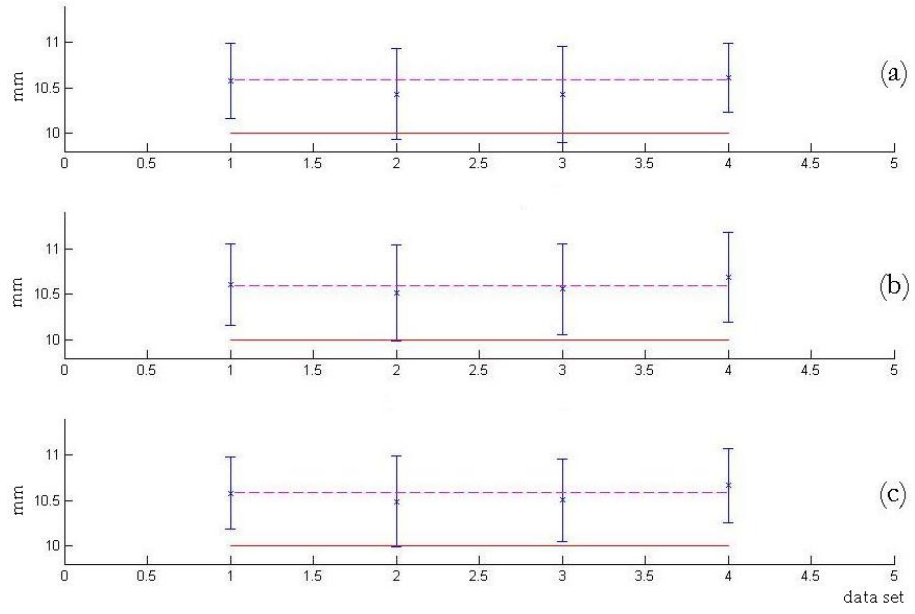

Figure A.5: Measurements at 10 mm axially in phantom. (a) Intensity method. (b) Geometry method. (c) Shape method. Solid line represents correct value. Dashed line represents correct value corrected for differing sound speed.

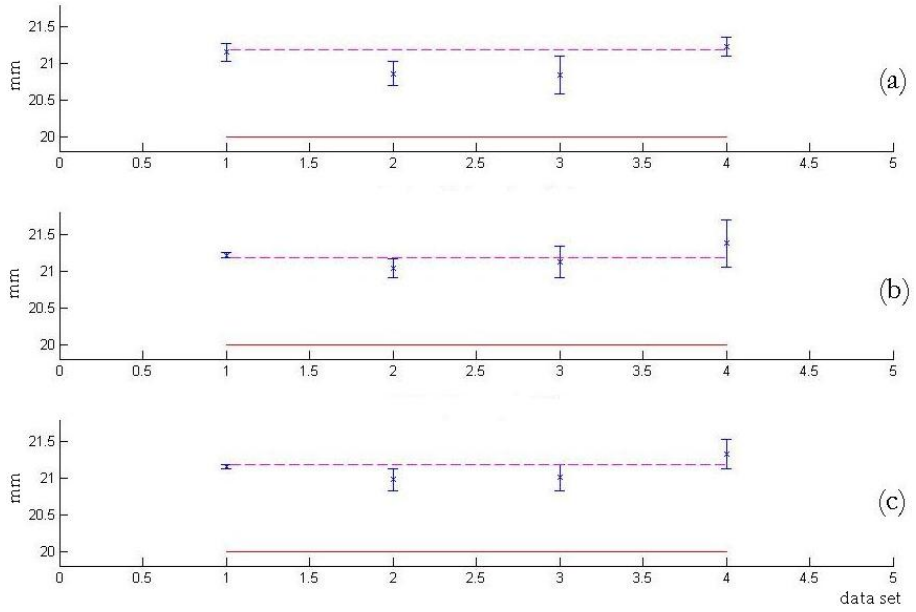

Figure A.6: Measurements at 20 mm axially in phantom. (a) Intensity method. (b) Geometry method. (c) Shape method. Solid line represents correct value. Dashed line represents correct value corrected for differing sound speed.

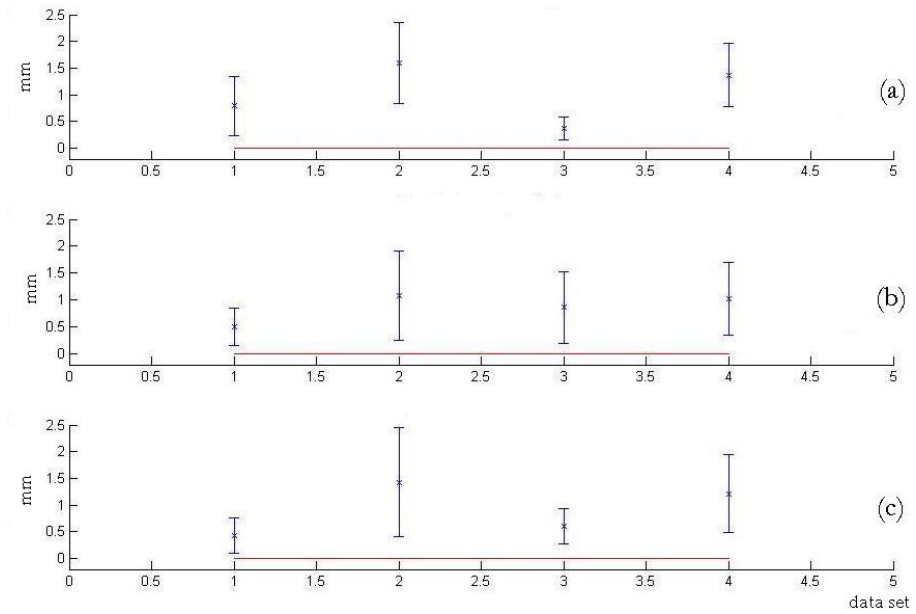

Figure A.7: Measurements at 0 mm laterally in liver. (a) Intensity method. (b) Geometry method. (c) Shape method. Solid line represents correct value.

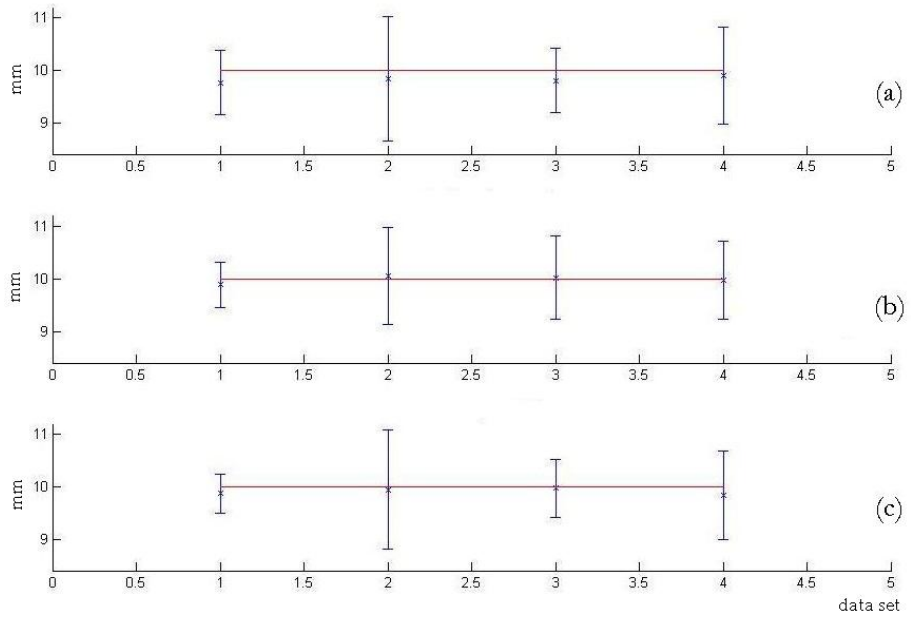

Figure A.8: Measurements at 10 mm laterally in liver. (a) Intensity method. (b) Geometry method. (c) Shape method. Solid line represents correct value.

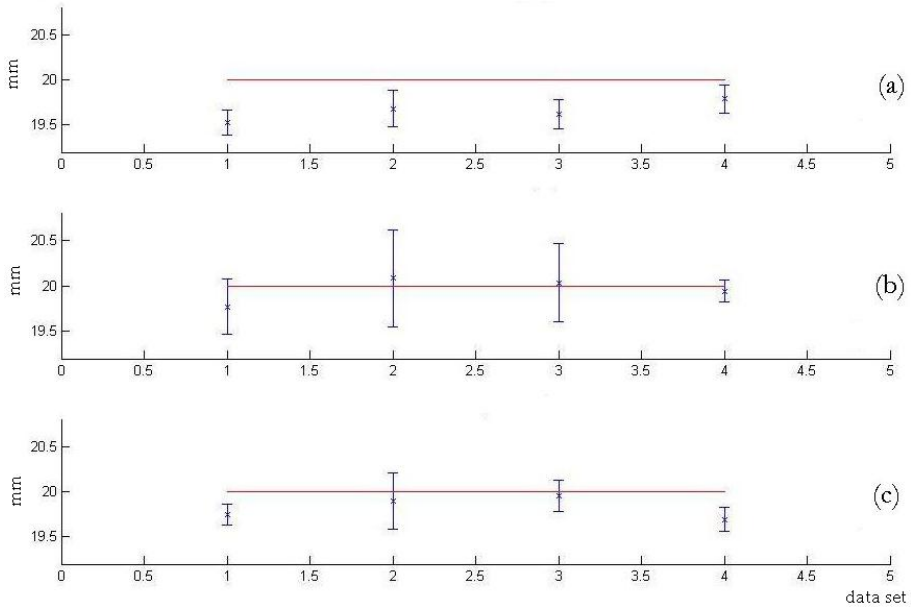

Figure A.9: Measurements at 20 mm laterally in liver. (a) Intensity method. (b) Geometry method. (c) Shape method. Solid line represents correct value.

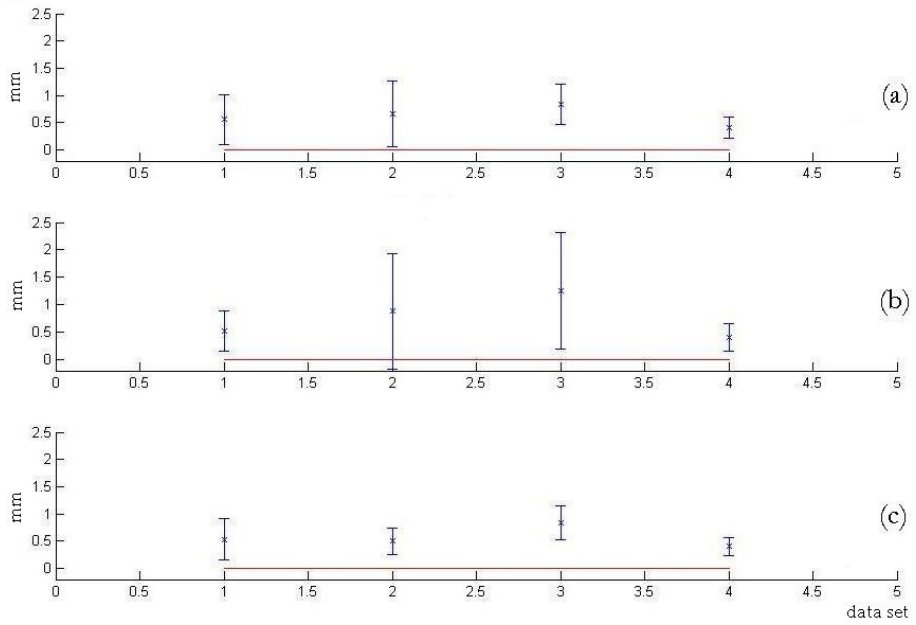

Figure A.10: Measurements at 0 mm axially in liver. (a) Intensity method. (b) Geometry method. (c) Shape method. Solid line represents correct value.

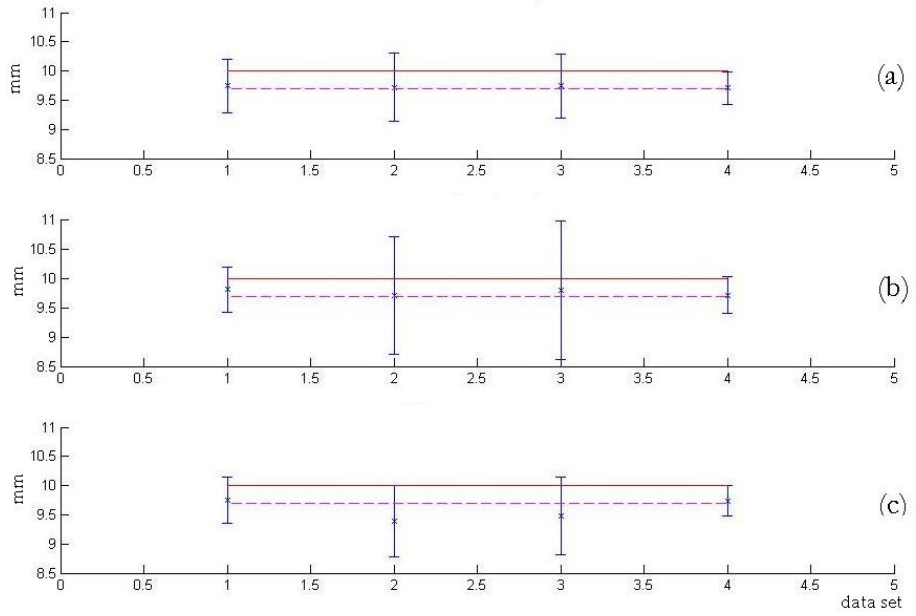

Figure A.11: Measurements at 10 mm axially in liver. (a) Intensity method. (b) Geometry method. (c) Shape method. Solid line represents correct value. Dashed line represents correct value corrected for differing sound speed.

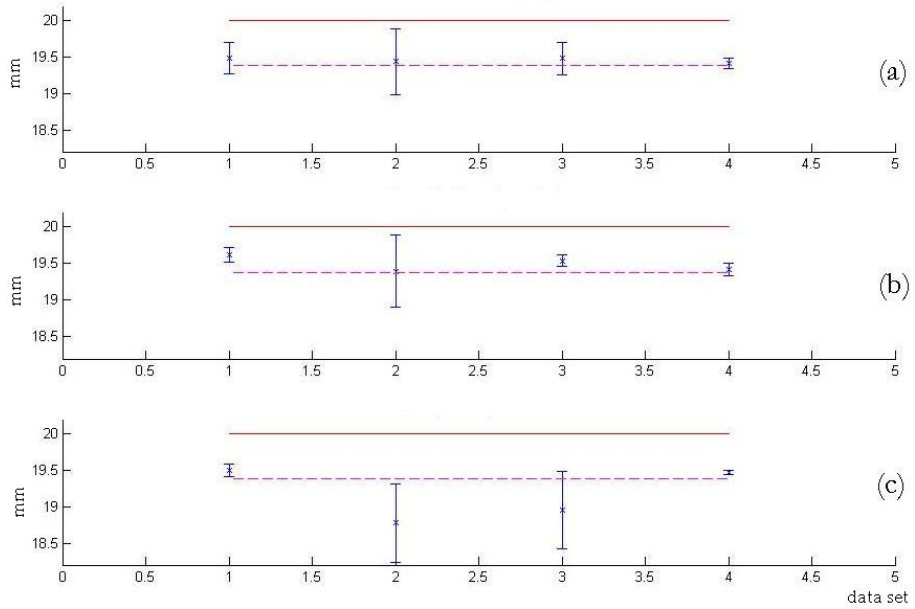

Figure A.12: Measurements at 20 mm axially in liver.(a) Intensity method. (b) Geometry method. (c) Shape method. Solid line represents correct value. Dashed line represents correct value corrected for differing sound speed.

Appendix B

Work Responsibilities

This thesis project was performed by two students from the Engineering Physics branch at Lund Institute of technology. The project started September 1st 2005 and ended February 10th 2006. The work load was equally divided between the participants. Table B.1 shows a more detailed list of the work responsibilities. The percentages are approximate.

Table B.1: The division of work between the two participants

Task	**Ulrika**	**David**
Experimental work	50%	50%
Image analysis	60%	40%
MatLab programming	30%	70%
Report writing	60%	40%
Miscellaneous	50%	50%

Experimental work includes producing the different phantoms, setting up the experimental environments, doing the experiments and evaluating the results.

Image analysis includes experimenting with different image analysis methods and finding an approach suitable for the ultrasound application.

Programming includes writing the three fibre position algoritms and data collecting and evaluating programmes.

Report writing includes research on related topics, generating images, figures and tables and writing.

Miscellaneous includes presentations, meetings and such.

Appendix C

Recipe for Candle Gel Phantom

The goal with this manufacturing procedure is to get as few air bubbles as possible.

1. Put an appropriate amount of candle gel in a glass jar or something similar.
2. Place the jar in an oven at 70°C and leave it there until all gel has melted. How long it takes depends on the amount of gel. A liter takes about three to four hours.
3. If an absorbing and/or scattering substance is to be added this should be done when the gel has melted. The substance should be carefully stirred into the gel. A tip is to use a warm stir rod since the gel hardens quickly if it gets in contact with something cold.
4. After the stirring the gel has probably hardened to some extent. It is therefore appropriate to put the glass jar back into the oven. At this time the box intended to hold the phantom should also be heated, for example by putting it in the oven with the gel.
5. After the second heating it is time to pour the gel into the box intended to hold the phantom. Try to pour slowly in one of the corners of the box.
6. Put the box back in the oven for five to six hours or longer. During this time most of the air bubbles will disappear. If glass pearls are used as scattering substance the box should not be heated for more than six hours since the glass pearls tend to sink.
7. Take the box out of the oven and scrape any bubbles on the surface to

the side, for example with a ruler.

8. Put the box in cold water, preferably 0°C.
9. Leave the box in the water until the whole phantom has hardened, for example over night.

If no oven is available a hot water bath can also be used. Try then to use a lid so that the phantom gets evenly distributed heat. Otherwise the gel tend to harden on the surface, making it hard to mix in any substances.

Appendix D

Meaurements on Magnetic Resonance Images

There was a general intrest among the supervisors to investigate whether optical fibres can be detected by *Magnetic Resonance Imaging*, MRI. A literature study was made which showed that experiments regarding this topic have been performed. Two articles were found on the subject[32;33].

Measurements were made in collaboration with the department of Magnetic Resonance Physics at Lund University Hospital. The camera used came from Siemens and had a homogeneous magnetic field of 3 Tesla.

Methods

Measurements were done on a candle gel phantom and a piece of liver. Different sequences were tested.

For the phantom measurements the sequence in table D.1 was used. For the liver measurements the sequence in table D.2 was used.

The fibre position algorithms developed in the project were tested on the MR images.

Results and Discussion

Figure D.1 shows a magnetic resonance image of the phantom and a corresponding ultrasound image. The fibres are clearly visible in the images.

Table D.1

Parameter	*Value*
Sequence	t1_se_cor_320_3mm
Scan time	9:02 min
Voxel size	0,4x0,4x4,0 mm
Phase oversampling	22%
FoV read	137 mm
FoV phase	75,0%
Slice thickness	4 mm
TR	600 ms
TE	9,7 ms
Averages	3
Concatenations	1
Filter	Elliptical filter
Coil elements	HS1, HS2, HS3, HS4
Matrix	245x384

Table D.2

Parameter	*Value*
Sequence	t1_se_cor_320_3mm
Scan time	18:00 min
Voxel size	0,4x0,4x4,0 mm
Phase oversampling	22%
FoV read	137 mm
FoV phase	75,0%
Slice thickness	4 mm
TR	600 ms
TE	9,7 ms
Averages	6
Concatenations	1
Filter	Elliptical filter
Coil elements	HS1, HS2, HS3, HS4
Matrix	245x384

Figure D.2shows an magnetic resonance image of the liver and a corresponding ultrasound image. The fibres are clearly visible in the MR image but not in the ultrasound image.

The MR images are not as grainy as the ultrasound images. The fibres in the MR images are well defined and not smeared. The main disadvantage is the time needed, the MR images took 9 and 18 minutes, respectively, to produce while the ultrasound images only took ~ 1 s.

Figure D.3 shows the three fibre position algorithms applied on a MR phantom image. The methods all give a likely position of the fibres. The shape method is a little bit off. This is probably due to it not being optimized for MR images.

Conclusions

The experiment showed that it is possible to find optical fibres in tissue with MR. It also showed that the methods developed for ultrasound images work on MR images as well.

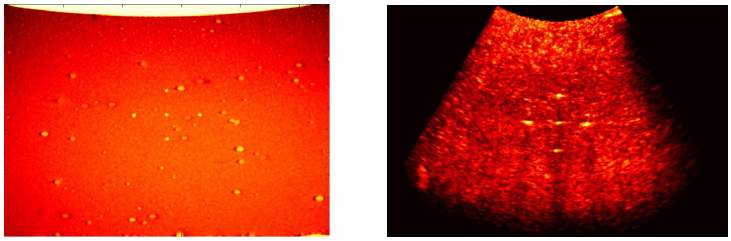

(a) Magnetic resonance image (b) Ultrasound image

Figure D.1: MR and ultrasound image of the phantom.

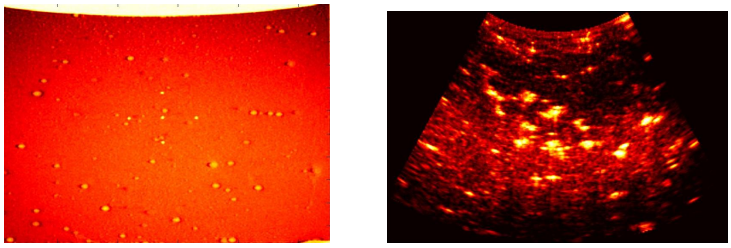

(a) Magnetic resonance image (b) Ultrasound image

Figure D.2: MR and ultrasound image of a liver sample.

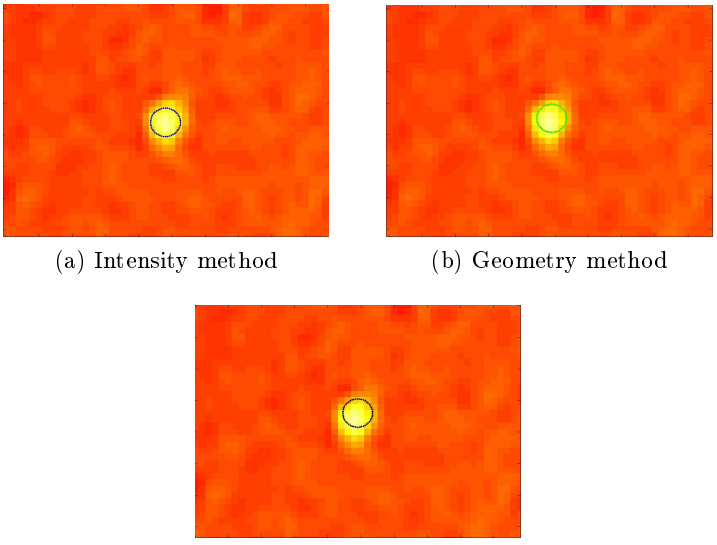

(a) Intensity method (b) Geometry method

(c) Shape method

Figure D.3: The fibre position algorithms applied on a MR phantom image.

Appendix E

Visit to a Brachytherapy Session

September 27th a visit was made to a brachytherapy session at the Oncology Clinic at Lund University Hospital. Dr. Ola Bratt was the physician in charge, Dr. Margrèt Einarsdòttir was assisting physician and Per Munck was the medical physicist. Two nurses and two anesthesiologists were also present.

The patient was under anesthesia, lying on an operating table with legs in an upright position exposing the perineum. A transrectal ultrasound probe was used to monitor the treatment. The probe was prepared for use by covering it with a protective coating. This coating had a pocket that was filled with ultrasonic gel to fill up the space between the probe and the rectum wall. The probe was inserted and the ultrasound scanner was configured to give optimal response.

The number of possible cross sections, planes, of the prostate was estimated. The planes were situated 5 mm apart. A series of pictures were captured, one in each plane. The scanner was connected to a laptop for further analysis and dosimetry calculations using VariSeed 7.1 (SeeDOS Ltd.). Dr. Ola Bratt marked the prostate boundary, urethra and rectum in each plane. This was used to make a 3D-view of the geometry of the prostate. Per Munck used the information to make dosimetry suggestions. The oncologist, Dr. Margrèt Einarsdòttir, then decided which to use.

A template was placed on top of the US probe. With help of X-ray and ultrasound two fixation needles were placed, one on each side of the urethra. The needles contained two barbs, one that stuck to the base of the prostate, and one that stuck to the skin. Then treatment needles with radioactive seeds inside were inserted. Usually needles that have to go in the furthest,

are placed first, and so on. During the placement, the dosimetry model was updated according to the actual positions of the seeds, so that the treatment dose was properly estimated. The physiscian and the physicist continously discussed the placement and placement order of the needles. The therapy session ended with another image collection of the planes and a x-ray image.

The prostate contains ridgid tissue and bleedings are not likely to stay within the gland. Local stricture can make it harder to place the needles, as they are long and thin and therefore bend easily.

Brachytherapy is used for treatment of T1-T2a tumours. The seeds contain ^{125}I with a half- life of 60 days. The seeds are not removed. Few side effects have been observed, the most common being stricture in the urethra 2-3 weeks after implantation.

The patient is hospitalized for approximately two days in total. The treatment is then followed up with PSA tests every three months the first year, every six months the second year and then once a year. The treatment costs about 100 000 sek which is roughly the same as the cost for other prostate cancer treatments, but in this case practically no convalescence time is needed.

Appendix F

MatLab Code